Microfluidic Hydrodynamic of Gas-Liquid flow in Single Microchannel and Porous Media with Microchannel Network

Yang, Shuo

2022

Document Version:
Publisher's PDF, also known as Version of record

Microfluidic Hydrodynamic of Gas-Liquid flow in Single Microchannel and Porous Media with Microchannel Network

SHUO YANG
DEPARTMENT OF ENERGY SCIENCES | FACULTY OF ENGINEERING | LUND UNIVERSITY

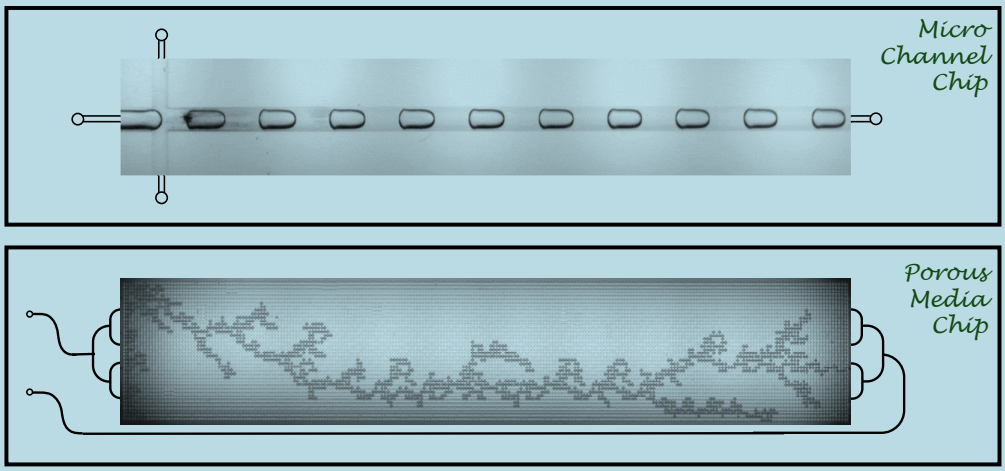

Microfluidic Hydrodynamic of Gas-Liquid flow in Single Microchannel and Porous Media with Microchannel Network

Microfluidic Hydrodynamic of Gas-Liquid flow in Single Microchannel and Porous Media with Microchannel Network

Shuo Yang

LUNDS UNIVERSITET
Lunds Tekniska Högskola

LICETIATE DISSERTATION

With permission of the Faculty of Engineering (LTH), Lund University, Sweden. To be defended on Friday 09 December 2022, at 13:15 AM in Lecture Hall KC:D at the Chermistry Centre, Naturvetarvägen 14, Lund, Sweden.

Thesis supervisor: Professor Johan Revstedt, Dr. Lei Wang, Dr. Zhen Cao

Faculty opponent: Professor Shervin Bagheri, Department of Applied Mechanics, Royal Institute of Technology, Stockholm, Sweden

Organization LUND UNIVERSITY	Document name LICENTIATE DISSERTATION
Department of Energy Sciences	Date of issue December 09, 2022
Author(s) Shuo Yang	Sponsoring organization China Scholarship Council

Title and subtitle

Microfluidic Hydrodynamic of Gas-Liquid flow in Single Microchannel and Porous Media with Microchannel Network

Abstract

In this thesis, a microfluidics platform with high-speed imaging system was built to investigate gas-liquid flow in single microchannel and interfacial instability in porous media with microchannel network:

The mass transfer of slug flow in the rectangular and square microchannels was experimentally studied by using water as liquid phase and CO_2 as gas phase. Depending on flow rates, flow patterns including slug flow, bubbly flow, and annular flow were observed in rectangular and square microchannels. Flow pattern map was proposed and compared with the maps in the literatures. By using digital image processing, the bubble volume especially deformed bubbles in rectangular and square microchannels was calculated based on 2D projection and 3D slicing, correspondingly. Scaling laws including important parameters of bubbles were derived to provide the guidance of microreactor design. Mass transfer coefficients were calculated based on bubble volume. The empirical correlations involving dimensionless numbers were fitted to precisely predict mass transfer coefficients. Further, to be universality, a semi-theoretical model considering length ratio of liquid and gas phases was developed to predict measured mass transfer coefficients in square microchannel precisely.

The gas-liquid displacement in porous media with microchannel network was experimentally investigated. By varying capillary numbers Ca and viscosity ratios M in a wide range, flow pattern involving viscous fingering (VF), capillary fingering (CF) and crossover zone (CZ) can be observed. Finger morphologies at breakthrough moment and steady state in three different flow regions was visualized. The main difference between VF and CF is that the gas stops invading in CF region after breakthrough, whereas in VF region gas can continue to expand until almost all the liquid phase is displaced. Invasion velocity, phase saturation and fingering complexity were quantified based on digital image processing. Fingering dynamical behaviors in different flow pattern before and after breakthrough was investigated. Time evolution of fingering displacement after breakthrough demonstrated an unobserved circle, consisting of new finger generation, cap invasion, breakthrough and finger disappearance. The circle repeats until steady state. Finally, local dynamical invasion behavior was studied and a stepwise way of gas invasion was exposed.

Key words:

mass transfer, slug flow, porous media, interficial instability, fingering displacement

Classification system and/or index terms (if any)

Supplementary bibliographical information	Language English
ISSN and key title ISSN 0282-1990 ISRN LUTMDN/TMHP-22/7108-SE	ISBN 978-91-8039-457-4 (print) 978-91-8039-458-1 (electronic)

Recipient's notes	Number of pages 59	Price
	Security classification	

Microfluidic Hydrodynamic of Gas-Liquid flow in Single Microchannel and Porous Media with Microchannel Network

Shuo Yang

LUNDS UNIVERSITET
Lunds Tekniska Högskola

Department of Energy Sciences

Faculty of Engineering (LTH)

Lund University, Lund, Sweden

www.energy.lth.se

Thesis for the degree of Licentiate of Philosophy in Engineering.

Division of Heat Transfer
Department of Energy Sciences
Faculty of Engineering (LTH)
Lund University
Box 118
SE-221 00 LUND
SWEDEN

978-91-8039-457-4 (print)
978-91-8039-458-1 (electronic)
ISRN: LUTMDN/TMHP-22/7108-SE
ISSN: 0282-1990

Printed in Sweden by Media-Tryck, Lund University
Lund 2022

Popular Science

Gas-liquid flow is ubiquitous in nature such as rainwater irrigation. It is an essential process in industrial applications, like chemical, petrochemical, pharmaceutical and food production, which are always companied by heat and mass transfer. The traditional instrument at the macro scale like stirred tank can't control heat and mass transfer precisely due to inadequate mixing. It will cause the waste of extra raw materials and energy. In response to this demand, microfluidics technology, also known as Lab-on-a-Chip, was developed. Microchannel is fabricated on the microchip, in which feeding fluid can be manipulated accurately, and thus the heat and mass transfer coefficients are significantly enhanced. However, the interaction between gas and liquid phases is complex and the mechanism of multiphase flow remains unclear. It is imperative to investigate gas-liquid flow in single straight microchannels to enhance the understanding of dynamical interaction and mass transfer between phases.

Porous media can be considered as microchannel networks, formed by interconnected pores. Gas-liquid fingering displacement in porous media widely exists in industrial and subsurface applications, such as fuel cells and geological carbon sequestration. The non-compact fingering structure resulting from interfacial instability has an important influence on extraction effectiveness and leakage risk. Therefore, it is essential to study the fingering dynamics in porous media. Especially, displacement process after breakthrough is hardly studied. Evolution after breakthrough need further exploration.

In this thesis, a microfluidics platform was built to test the flow in microscale. In the first step, gas-liquid flow in straight rectangular and square microchannels was investigated by using water as liquid phase and N_2 and CO_2 as gas phase. Flow pattern was captured by a high-speed imaging system and the recorded images were processed by digital image technology. Flow pattern map was proposed and compared with the map in literatures. Bubble volume especially deformed bubbles was measured by 2D projection and 3D slicing methods. Scaling laws involving important parameters in microreactor were proposed to provide the guidance of microreactor design. Based on bubble volume, mass transfer coefficient was calculated. The effect of flow rate on mass transfer was investigated. Empirical correlations and semi-theoretical model were derived to predict mass transfer coefficient.

In the following step, the gas-liquid fingering displacement in porous media with microchannel network was investigated by using different concentrations of glycerol solutions as liquid phase and air as gas phase. Flow regime was compared with the region boundaries in phase diagram of literatures. Fingering pattern morphologies at the breakthrough moment and at the steady state were captured. The fingering displacement process was quantified by the fingering cap velocity, saturation and fractal dimension based on digital image process technique. To reveal the underlying mechanism of interfacial instability, dynamical evolution of fingering before and after breakthrough was analysed. Further, local invasion dynamics in porous media was studied by the macro lens.

Abstract

In this thesis, a microfluidics platform with high-speed imaging system was built to investigate gas-liquid flow in single microchannel and interfacial instability in porous media with microchannel network:

The mass transfer of slug flow in the rectangular and square microchannels was experimentally studied by using water as liquid phase and CO_2 as gas phase. Depending on flow rates, flow patterns including slug flow, bubbly flow, and annular flow were observed in rectangular and square microchannels. Flow pattern map was proposed and compared with the maps in the literatures. By using digital image processing, the bubble volume especially deformed bubbles in rectangular and square microchannels was calculated based on 2D projection and 3D slicing, correspondingly. Scaling laws including important parameters of bubbles were derived to provide the guidance of microreactor design. Mass transfer coefficients were calculated based on bubble volume. The empirical correlations involving dimensionless numbers were fitted to precisely predict mass transfer coefficients. Further, to be universality, a semi-theoretical model considering length ratio of liquid and gas phases was developed to predict measured mass transfer coefficients in square microchannel precisely.

The gas-liquid displacement in porous media with microchannel network was experimentally investigated. By varying capillary numbers Ca and viscosity ratios M in a wide range, flow pattern involving viscous fingering (VF), capillary fingering (CF) and crossover zone (CZ) can be observed. Finger morphologies at breakthrough moment and steady state in three different flow regions was visualized. The main difference between VF and CF is that the gas stops invading in CF region after breakthrough, whereas in VF region gas can continue to expand until almost all the liquid phase is displaced. Invasion velocity, phase saturation and fingering complexity were quantified based on digital image processing. Fingering dynamical behaviors in different flow pattern before and after breakthrough was investigated. Time evolution of fingering displacement after breakthrough demonstrated an unobserved circle, consisting of new finger generation, cap invasion, breakthrough and finger disappearance. The circle repeats until steady state. Finally, local dynamical invasion behavior was studied and a stepwise way of gas invasion was exposed.

Keywords: mass transfer, slug flow, porous media, interfacial instability, fingering displacement

Acknowledgments

Time flies. I'm halfway through my PhD research. It is a tough journey always with confusion and frustration. I hate it but enjoy and appreciate it. Firstly, I appreciate myself to have the courage to come to Sweden, far away from home, to take the PhD. I still remember the rain night I got off the train in Lund C with two big suitcases. I started this journey with anticipation. PhD research was not always smooth. I often experienced setbacks and felt like giving up. Thanks to many people who helped and inspired me. I would like to express my gratitude to all of you.

First and foremost, I want to send my deepest gratitude and respect to my supervisor, Professor Johan Revstedt and former supervisor, Professor Zan Wu. Thank you, Zan, for taking the role as the supervisor for the first year and for leading me into the PhD journey and teaching me how to do scientific research. Your wisdom and attitude toward study have been inspiring me. Thank you, Johan, for taking over the responsibility of supervisor and providing guidance for my research, especially assisting me in finishing the licentiate defense step by step. You always provided effective advice and encouraged me whenever I needed help. Apart from the work, you both cared about my life kindly. Without you, I would not be able to carry out my PhD project smoothly. I appreciate having both of your guidance over the past two years. I will carry your expectations forward for the next two years of PhD. Thank you very much again.

Thank you, my co-supervisors, Lei Wang and Zhen Cao. Thank you, Lei, for providing useful suggestion for my research, especially the design of microchip holder. Thank you, Zhen, also my close friend. You always gave me a hand in my life. In terms of experiments, you often suggested effective solutions and answered my questions patiently. I enjoy doing experiment with you in M-hust and working in our office of KC.

Especially, I would like to appreciate my former colleague, Gaopan Kong. You led me to build the microfluidics platform and develop the experimental method at the beginning of PhD. Thank you for your recommendation for academic visiting. In addition, I would like to thank Hongxia Li who offered me a lot of help in the field of porous media. Your intelligence and work attitude are worth learning for me.

I want to post a big **Thank you** to all my nice colleagues in the department, Danan, Yuxiang, Zhan, Yong, Hongwei, Arvid, Gustav, Himani, Thommie, Alexandra, Francesco, Joe, Guillaume, Dequan, Xiaoqiang, Miao … all of you. Thank you for the interesting discussion in the lunchroom and the party afterwork. Thank Danan for assisting me with the data processing code. Encouragement of you and Yuxiang helped me get out of trouble. I enjoy every moment of working with all of you.

I would like to thank the technicians in the department, Anders Olsson. Thanks for helping me fabricate the experimental component. I also want to thank the administrative staffs, Catarina Lindén and Isabelle Frej. Thanks for the help with student registration, course registration and expense reimbursement.

For financial support, I would like to appreciate the China Scholarship Council (CSC) which granted me the PhD scholarship for my living and accommodation in Sweden, and the Royal Physiographic Society of Lund which supported me to attend the conferences.

Last, I would like to thank my family, the most important people in my life: My father 杨经超, my mother 吴莹, my sister 杨海冰, my grandfather 吴日胜, my grandmother 刘雪娇, my uncle 吴小锐. I really appreciate your care and support in my life. Every time I feel like giving up, your encouragement keeps me going. Thanks to your selfless love and support, I can feel free to explore the world and pursue my dream.

List of Publications

Publications included in the thesis:

Paper i: Experimental study of gas-Liquid Mass transfer in a rectangular microchannel by digital image analysis method
***Shuo Yang**, Gaopan Kong, Zan Wu**
ASME International Mechanical Engineering Congress and Exposition, 2021, Nov 1 (Vol. 85666, p. V010T10A040).

In this paper, I built up the microfluidic platform together with Gaopan Kong. I did the experiments, analyzed the data and wrote the paper. Gaopan and Zan Wu helped with technical suggestions, gave feedback and proofread the paper.

Paper ii: Mass transfer and modeling of deformed bubble in square microchannel based on 3D slicing technique
***Shuo Yang**, Gaopan Kong, Zhen Cao, Zan Wu[*]*
(manuscript in preparation).

In this paper, I built up the microfluidic platform together with Gaopan Kong. I did the experiments, analyzed the data and wrote the paper. Gaopan Kong, Zhen Cao and Zan Wu helped with technical suggestions, gave feedback and proofread the paper.

Paper iii: Hydrodynamics of gas-liquid displacement in porous media: fingering pattern evolution at the breakthrough moment and the steady state
***Shuo Yang**, Gaopan Kong, Zhen Cao, Zan Wu[*], Hongxia Li[**]*
Advances in Water Resources, 2022, 104324.

In this paper, I built up the test rig of porous media. I did the experiments, analyzed the data and wrote the paper. Gaopan Kong, Zhen Cao, Hongxia Li and Zan Wu helped with technical suggestions, gave feedback and proofread the paper.

Nomenclature

a	specific interfacial area (m^{-1})
A_B	interface area of bubble (m^2)
A_{BT}	fingering area at breakthrough moment (m^2)
A_{bd}	cross-sectional area of bubble (m^2)
A_{body}	interface area of bubble body (m^2)
A_C	cross-sectional area of microchannel (m^2)
A_{front}	interface area of bubble front cap (m^2)
A_{rear}	interface area of bubble rear cap (m^2)
A_{SS}	fingering area at steady state (m^2)
$A(z_B)$	cross-section area on slice (m^2)
Ca	Capillary number
Ca_B	Capillary number of bubble
Ca_T	Capillary number of both phases
$C_{L,b}$	concentration at the liquid bulk (mol/L)
$C_{L,i}$	concentration at the interface (mol/L)
d	distance between centroid of upper front cap and the revolution axis (m)
D	depth of channel cross-section of porous media chip (m)
D_{dif}	diffusivity (m^2/s)
D_h	hydraulic diameter (m)
FD_B	Fractal dimension at breakthrough moment
FD_S	Fractal dimension at steady state
H	Henry constant in dimensionless form
H_B	depth of bubble (m)
H_C	depth of microchannel (m)
j_B	bubble velocity (m/s)
j_G	superficial gas velocity (m/s)
j_L	superficial liquid velocity (m/s)
j_T	total superficial velocity (m/s)
k_G	overall mass transfer coefficient of gas phase (m/s)
k_L	overall mass transfer coefficient of liquid phase (m/s)
$k_L a$	volumetric mass transfer coefficient (1/s)
L	length of porous media domain (m)
L_{body}	length of bubble body (m)
$L_{boundary}$	length of the boundary of the upper front cap (m)
L_C	length of unit cell (m)
L_f	length of bubble film (m)
L_{front}	length of bubble front cap (m)
L_G	length of gas slug/bubble (m)

L_L	length of liquid plug (m)
L_{rear}	length of bubble rear cap (m)
M	viscosity ratio between the invading phase and defending phase
M_G	transferred mass in mole of gas phase (mol)
M_L	transferred mass in mole of liquid phase (mol)
N	number of boxes
N_z	number of slices
P	pressure (Pa)
ΔP	pressure drop (Pa)
$P_{\text{atmosphere}}$	atmospheric pressure (Pa)
P_{bd}	perimeter of bubble cross-section (m)
P_C	perimeter of microchannel cross-section (m)
$P_{G,b}$	partial pressure at the gas bulk (Pa)
$P_{G,i}$	partial pressure at the interface (Pa)
$P(z_B)$	interfacial perimeter on slice (m)
Q_G	gas flow rate (mL/h)
Q_L	liquid flow rate (mL/h)
r_t/r	curvature radius (m)
Re_B	Reynolds number of bubble
Re_G	Reynolds number of gas phase
Re_L	Reynolds number of liquid phase
Re_T	Reynolds number of total phases
S_B	saturations at breakthrough moment
Sc_L	Schmidt number of liquid phase
S_{front}	projected area of the upper front cap (m^2)
Sh	Sherwood number
S_S	saturations at stead state
t	time (s)
T	elapsed time (s)
T_B	elapsed time for the finger cap to reach breakthrough time (s)
T_S	elapsed time for the finger cap to reach steady state (s)
U_{cap}	velocity of finger cap (m/s)
u_i	Darcy velocity of the invading phase (m/s)
V_B	bubble volume (m^3)
V_{body}	volume of bubble body (m^3)
V_{front}	volume of bubble front cap (m^3)
V_{rear}	volume of bubble rear cap (m^3)
V_C	volume of cell (m^3) $V_C = W_C^2 L_C$
W	width of porous media domain (m)
W_B	width of bubble (m)
W_C	width of microchannel (m)

W_S	width of straight channel in porous media (m)
W_{C1}	width of throat 1 in porous media (m)
W_{C2}	width of throat 2 in porous media (m)
$\overline{W_B}$	average width of bubble (m)
X_{Cap}	location of finger cap (m)

Greek symbols

δ	width of body film (m)
θ	contact angle
θ_R	receding contact angle
μ	dynamic viscosity (Pa·s)
μ_i	dynamic viscosity of the invading phases (Pa·s)
μ_d	dynamic viscosity of the defending phases (Pa·s)
ρ	density (kg/m^3)
σ	surface tension (N/m)
σ_d	surface tension of dispersed phase (N/m)
Φ_B	bubble volume fraction
Δ	resolution scale

Abbreviations

CF	capillary fingering
CZ	crossover zone
GCS	geological carbon storage
GDL	gas diffusion layer
VF	viscous fingering

Table of Contents

CHAPTER 1

Introduction

1.1 Background

Gas-Liquid flow

Gas-liquid two-phase flow widely occurs in many industrial applications, such as chemical, petrochemical, pharmaceutical and food production. These are usually accompanied by heat and mass transfer processes such as chemical reaction, separation, absorption, extraction, cooling, heating, detection, etc. The traditional instrument, e.g., gas column, plate, stirred tank, gas-liquid reactors, fluidized beds and fluid transfer pipelines, has been developed to achieve these processes. At the macro scale, the control of mass and energy cannot reach a high precision by these instruments. Increase in by-products causes the waste of raw materials and energy. Inadequate mixing of reactants in a large reaction chambers increases the diffusion length. Therefore, they all have the same disadvantage of low mass or heat transfer coefficient. However, high precision can be achieved at microscale and submicron scale. Microfluidics was developed to enable such special processes that require high precision.

Microfluidics

Microfluidics is an advanced technology that precisely controls and manipulates micro-scale fluids, also known as Lab-on-a-Chip or microfluidic chip technology. Microfluidics originates from a concept called Miniaturized Total Analysis System (μTAS) that was first proposed by Manz and Widmer et al.[1] in 1990. With the development of micromachining technology, we can fabricate various microstructure units such as micron to submillimeter fluid channels, reaction and detection chambers, filters and sensors on the chip. Various materials, e.g., glass, quartz, ceramic, metal, polymer and composite, have been developed to fabricate microchips by using micromachining techniques, such as wet and dry etching, MEMS, micro-mechanical cutting, imprinting, lithography, embossing and advance micro-3D printing. Fluids can be manipulated precisely in the micron-scale space through fluid control or analytical instruments. The process, e.g., chemical reaction, separation, absorption

and cell culture, can be finished automatically. Therefore, the potential development prospects of microfluidics are gradually being valued by academia and industry.

In the field of chemical and pharmaceutical, the microfluidic chip is used as a modular microreactor shown in Figure 1-1 (a), by carrying out combinatorial chemical reactions or combining droplet technology [2]. Microscale channels in microchips can achieve accurate feed control, enhanced mixing, fast reaction and side-reaction limitation. Energy and raw material savings as well as high product purity enable the microchips to be used for drug synthesis, or for high-level synthesis of nanoparticles, microspheres, and crystals. And even a kind of "chemical factory or pharmaceutical factory on a chip" can be expected.

In the field of biomedicine, microfluidic bioreactor enables long-term culture and monitoring of extremely small populations of bacteria. As shown in Figure 1-1 (b), micro-fermentor systems can accelerate the process of strain screening and evaluation [3]. Besides, the clinical analysis can be integrated on a microchip in Figure 1-1 (c) [4]. In recent years, integrated functions of microfluidic chips are used to simulate the smallest functional units in human organs and realize drugs as shown in Figure 1-1 (d) [5]. The technology, called organ-on-a-chip, is used to understand and evaluate the effects of diseases, drugs, chemicals and food on humans. Organ-on-a-chip was selected as one of the top ten emerging technologies of 2016 in the world economic forum.

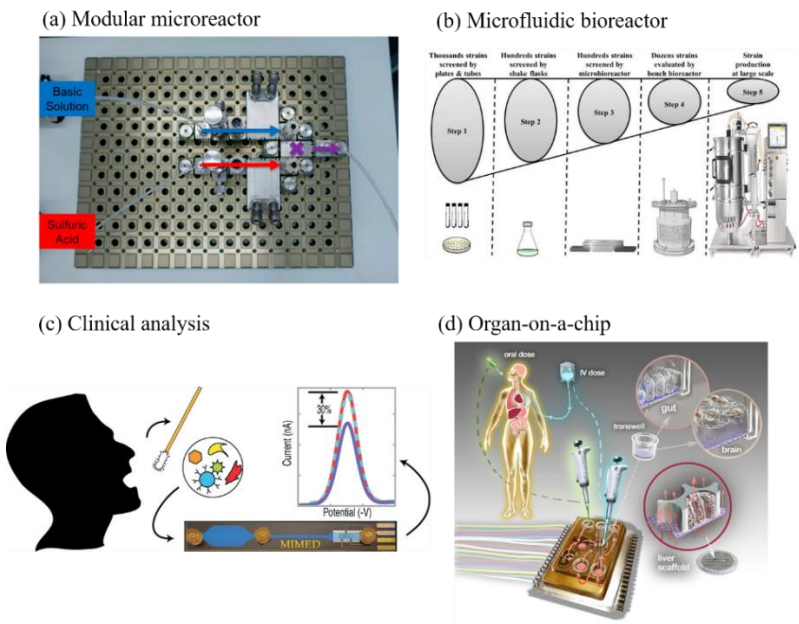

Figure 1-1 application of microfluidics: (a) modular microreactor [2]; (b) microfluidic bioreactor[3]; (c) clinical analysis[4]; (d) organ-on-a-chip [5]. (Reprint by permission from the publisher)

Single straight microchannel

Gas-liquid flow in a single straight microchannel, as the basic unit of a complex microfluidic chip, is fundamental and often addressed research topic[6]. The flow at the microscale is laminar and the straight microchannel can guarantee a stable flow. At the microscale, the effect of gravity on gas-liquid flow can be ignored. The gas-liquid flow in the straight microchannel is mainly controlled by the viscous force, surface tension, capillary force and inertial force. In practical industrial applications, one single microchannel is not sufficient to achieve complex reaction process. As shown in Figure 1-1 (d), multiple microchannels of different types are often required. Due to the limited area of a microchip, using meandering microchannels is often an compromise. However, Dean vortices and other centrifugal effects then need to be considered [7].

Porous media with microchannel networks

Porous media can be regarded as microchannel networks, formed by interconnected pores. The definition of porous media is solid object with connected holes, where the liquid or gas flow through. Porous media is ubiquitous in our lives and nature, e.g., sedimentary rock underground, rain-moistened soil, babies' nappy, water uptake in plants and gas exchange in lungs.

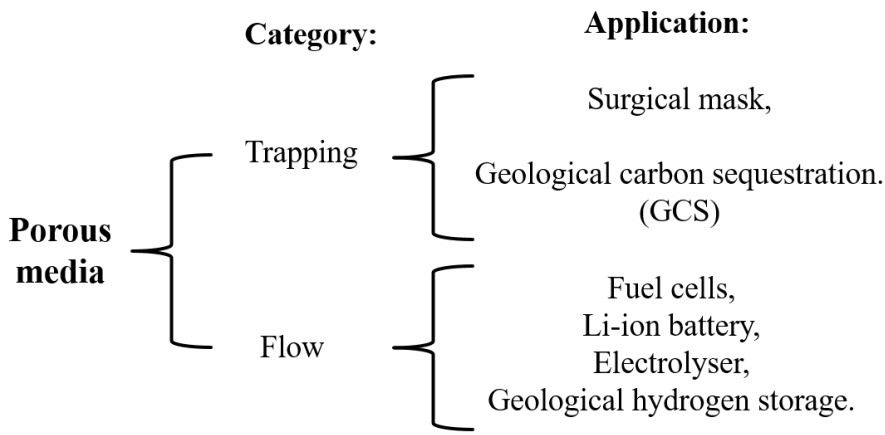

Figure 1-2 Category and industrial application of porous media.

Gas-liquid displacement in porous media is an essential process in many applications ranging from small scales, e.g., industrial processes, to large scales, e.g., terrestrial/extraterrestrial subsurface resource extraction and storage. According to the flow motion in porous media, porous media can be divided into 2 categories shown in Figure 1-2. One category is that the fluid is surrounded by another fluid and they both are trapped in the pore space. The most classic application is geological carbon sequestration (GCS). There are a lot of porous spaces between the underground rocks, which are filled with saline water and gas. Carbon dioxide

can be captured from industrial processes, then compressed and injected into the pore space of the rock underground, where it can be stored in the reservoir permanently. Another example is surgical masks with porous media layers, where the water droplets containing viruses cannot penetrate the mask while the air will pass through. The second category is that all fluids can fully flow over a wide range of saturation. Little fluid is trapped in the porous media. It plays a significant role in energy fields, such as gas diffusion layer (GDL) in a fuel cells, Li-ion batteries and electrolysers. Pore space of rock underground also can be used to store hydrogen. As the cleanest energy source, hydrogen is promoted as a reliable, next-generation fuel. However, storage issues have hindered its development. Geological hydrogen storage is considered as the most effective way. Hydrogen can be safely and temporarily stored in rock space underground.

More generally, such process will occur in the myriad fields of science and technology where fluids pass through porous materials. Therefore, the research on gas-liquid displacement process in porous media is greatly meaningful to reveal the dynamical behavior and fluid-mechanical forces.

1.2 Objectives and methodologies

As described above, microfluidic widely exists in the field of chemical, pharmaceutical, biomedicine and subsurface. Extensive work has been devoted to gas-liquid flow in the microchannel and porous media. But there are still some unknown phenomena and mechanisms to be explored, in terms of the calculation method of the mass transfer coefficient of deformed bubbles in microchannels and the dynamical evolution of fingering displacement after breakthrough in porous media. Therefore, the initial objectives were set as follow:

Single straight microchannel

1. Hydrodynamics of gas-liquid flow in straight microchannels with square and rectangular cross-sections will be studied by using different concentrations of glycerol solutions as the liquid phase and N_2 and CO_2 as the gas phase.
2. Flow pattern map will be drawn and compared with the map proposed by literatures.
3. Volume of bubbles especially deformed bubbles in rectangular and square microchannels will be measured based on 2D projection and 3D slicing methods, separately. The mass transfer coefficient will be calculated on the base of bubble volume.
4. Scaling laws of bubble volume, velocity and volume fraction will be derived to characterize the micro-reactors.
5. Empirical correlations and a theoretical model were derived to predict mass transfer coefficient.

Porou media:

1. Gas-liquid displacement in porous media will be investigated by using different concentrations of glycerol solutions as the liquid phase and air as the gas phase.
2. Flow regime phase diagram will be drawn and compared with the region boundaries proposed by literatures.
3. Fingering displacement morphologies will be visualized at breakthrough moment and steady state by using the high-speed imaging system.
4. Quantitative analysis of the invasion velocity, area and complexity will be conducted based on the digital image process technique.
5. The complete dynamical fingering evolution process before and after breakthrough will be explored to reveal the underlying mechanism of fingering dynamics.
6. To enhance the understanding of the local fingering invasion dynamics in porous media, the local drainage process will be observed and analyzed by using the macro lens.

CHAPTER 2

State-of-the-Art Literature Review

Flow in microscopic space is a complex process. Due to its broad application prospects, gas-liquid flow at the microscale has been a hot research topic. This chapter reviews the progress of mass transfer of gas-liquid flow in microchannels and gas-liquid displacement in porous media over the past decades.

2.1 Microchannel

In order to meet different application conditions, various cross-sectional shapes of microchannels have been applied, such as circular, square, rectangular, trapezoidal and so on. Based on the number and mixing degree of feed streams, the number of inlets and configuration of junctions both need to be customized. Figure 2-1 demonstrates the different configurations of mixing junctions at the entrance of the microchannels, including cross-shaped junction, cross Y-junction, T-junction, Y-junction, cross flow T-junction and co-flow. Different mixing junctions can produce different mixing degrees of fluids, which will generate different flow patterns [8].

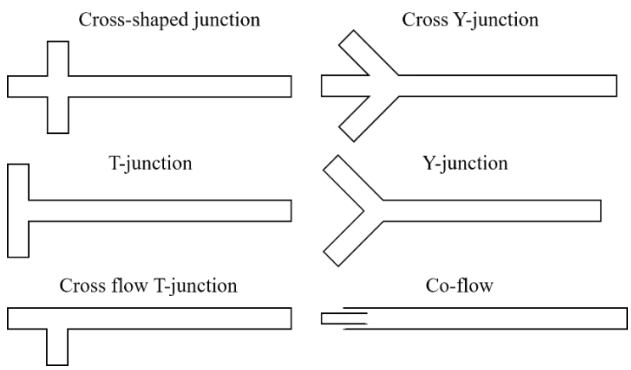

Figure 2-1 Junction configuration of microchannel.

2.1.1 Flow pattern

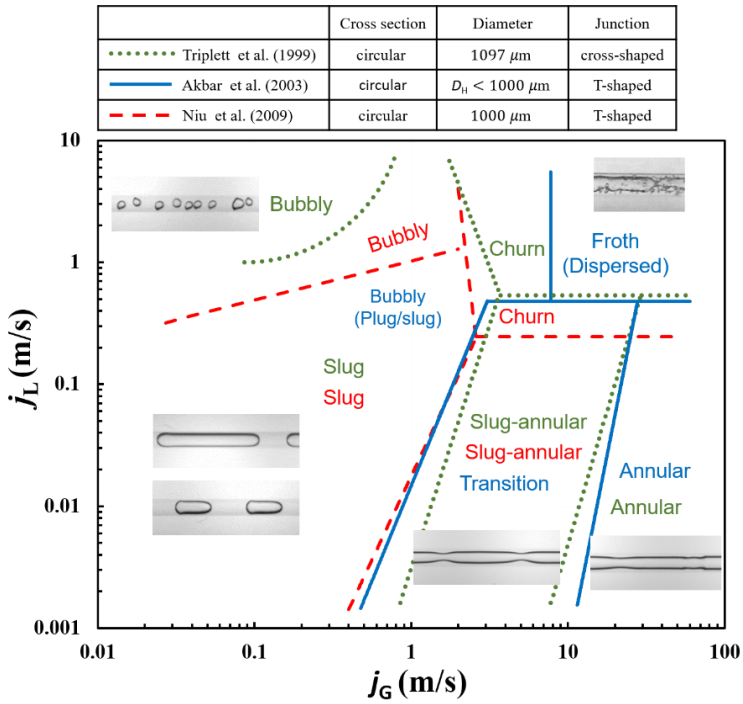

Figure 2-2 Comparison of the transition lines in gas-liquid flow pattern maps [9-11] and the flow pattern in different regions. (superficial gas velocity j_G and superficial liquid velocity j_L are calculated by the flow rate divided by the channel cross-sectional area, i.e., Q_G/A_C and Q_L/A_C. Reprint of churn image [9] by permission from the publisher)

Over the past few decades, many studies focus on the exploration of gas-liquid flow patterns. The flow pattern map including different flow regimes may be firstly proposed by Baker[12], based on superficial gas and liquid velocities. As shown in Figure 2-2, five types of flow patterns were found, including bubbly, slug (plug), churn (froth/dispersed), slug-annular (transition) and annular. Although they were named differently in literatures, they share some common characteristics:

- Bubbly flow. At the low j_G and high j_L, the irregularly shaped bubbles are dispersed in liquid phase and they do not flow in a horizontal line. Besides, the coalescence of bubbles may happen.
- Slug (plug) flow. Slugs with different lengths are generated and the shorter slug has a bullet shape. Due to the low j_G and j_L, the flow is stable. The distance between the slug and the size of slug are uniform.
- Slug-annular (transition) and annular flow. With the increase of j_G, the gas phase merges and thus elongated bubbles are generated. They are surrounded by a thin

liquid film. The fluctuations occur at the interface but are not enough to block the bubbles.

- Churn (froth/dispersed) flow. At the high j_G and j_L, disruption resulting from periodical flooding-type churning waves will lead to unstable slug flow.

The research on gas-liquid flow patterns transition can help predict flow patterns. Many studies proposed flow pattern transition lines to distinguish the different flow pattern transitions. Figure 2-2 shows the classical and popular transition lines in the flow pattern map reported by Triplett et al.[9], Akbar et al.[10] and Niu et al.[11]. Because their map was based on limited experimental data and different geometers of microchannel, there are disagreements with boundaries. The transition line from slug to bubbly proposed by Triplett et al.[9] is curved, while the one proposed by Niu et al.[11] is straight. In particular Akbar et al.[10] didn't distinguish bubbly and slug flow. At the higher superficial gas and liquid velocities, Akbar et al.[10] defined the regime as froth (dispersed) flow, while Triplett et al.[9] and Niu et al.[11] defined as churn flow. Their boundaries between churn and the other four flow regimes are not consistent. However, the boundaries between slug-annular and annular as well as between slug to slug-annular coincide reasonably well. It should be noted that Niu et al.[11] didn't distinguish the slug-annular and annular flow regime due to different flow pattern definitions.

2.1.2 Mass transfer

Mass transfer between dispersed phases (bubble/slug) and continuous phase (liquid) is the imperative process in microreactors. In single-phase flow, a classical Poiseuille flow profile with a maximum velocity on the center and a minimum velocity near wall is generated. In two-phase flow, the Poiseuille velocity profile is destroyed as shown in Figure 2-3 (b), because the flow speed of the dispersed phase is lower than the maximum velocity. Therefore, the recirculation is generated in both phases, as shown in Figure 2-3 (a). Recirculation can refresh the concentration near the gas-liquid interface. It is the recirculation that leads to the intensification of mass transfer, which was validated by using micro-PIV and CFD simulation in Figure 2-3 (c,d).

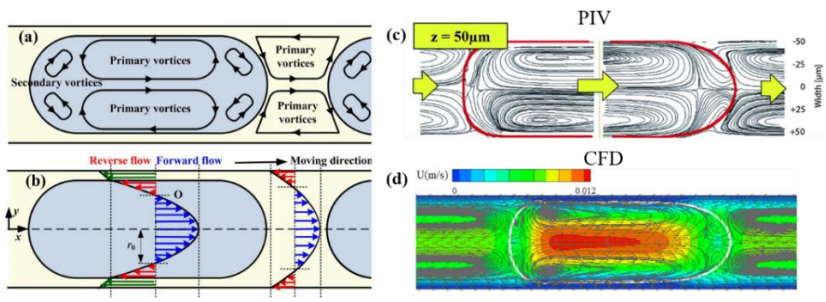

Figure 2-3 (a,b) Schematic diagram of recirculation [13]; (c,d) velocity profile from experimental Micro-PIV [14] and CFD simulation [15]. (Reprint by permission from the publisher)

Mass transfer from dispersed phase to continuous phase is described based on two-film theory, which is a classical theory of mass transfer process at gas-liquid interface, proposed by Whitman [16]. It simplifies the entire interphase mass transfer process as the molecular diffusion process of the component through two effective films. As shown in Figure 2-4, there exists stable gas stagnation layers (gas film) and liquid stagnation layers (liquid film) on both sides of the gas-liquid interface, respectively. The gas and liquid phases at the interface are in equilibrium. No mass transfer resistance is assumed at the phase interface. Besides, no mass transfer resistance is also assumed in the gas and liquid bulk outside the membrane layer, which means the concentration gradient (or partial pressure gradient) is zero. Therefore, the mass transfer coefficient can be expressed as:

As for gas phase:

$$\frac{dM_G}{dt} = k_G A_B (P_{G,b} - P_{G,i}) \tag{2-1}$$

As for liquid phase:

$$\frac{dM_L}{dt} = k_L A_B (C_{L,i} - C_{L,b}) \tag{2-2}$$

Here, k_G and k_L are the overall mass transfer coefficient of gas phase and liquid phase, respectively. M_G and M_L are the transferred mass in mole of gas phase and liquid phase, respectively. A_B is the gas-liquid interface area. $P_{G,b}$ and $P_{G,i}$ are the partial pressure at the gas bulk and interface, respectively. $C_{L,b}$ and $C_{L,i}$ are the concentration at the liquid bulk and interface, respectively. Smaller bubbles can have more contact area with liquid phase per unit volume, which enhances mass transfer. The specific interfacial area a characterizes the ratio of surface area A_B and volume of cell V_C, which has an important influence on mass transfer coefficient. Therefore, most literatures focus on the overall mass transfer coefficient of liquid phase k_L (unit: m/s) and volumetric mass transfer coefficient $k_L a$ (unit: 1/s).

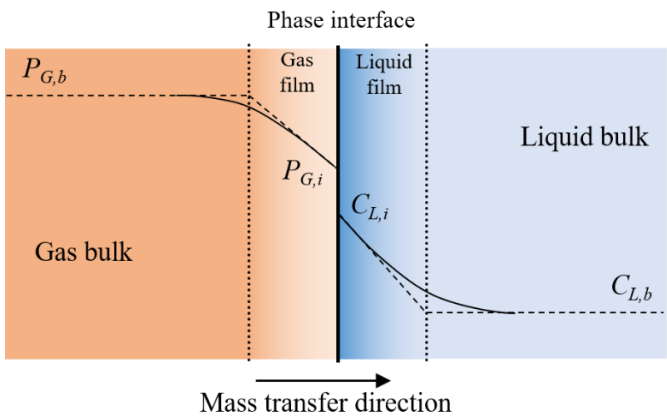

Figure 2-4 Schematic diagram of two film theory.

As shown in Figure 2-5, the unit cell consists of one slug (bubble) and one plug (liquid). It is reasonable to assume the mass transfer from gas to liquid phase only happens in a single unit cell, which means there is no mass transfer between unit cells. Due to mass conservation, the transferred mass in mole of gas phase and liquid phase is equivalent: $\frac{dM_G}{dt} = -\frac{dM_L}{dt}$. The volume of bubble decreases along the microchannel because of mass transfer, as shown in Figure 2-5.

According to ideal gas law, the mole mass of bubble can be represented as:

$$M_G = \frac{P_B V_B}{RT} \tag{2-3}$$

Substituting Equation (2-3) into Equation (2-2), the overall mass transfer coefficient of liquid phase k_L can be calculated by bubble volume change rate:

$$k_L = -\frac{1}{RTA_B(C_{L,i}-C_{L,b})}\frac{d(P_B V_B)}{dt} \tag{2-4}$$

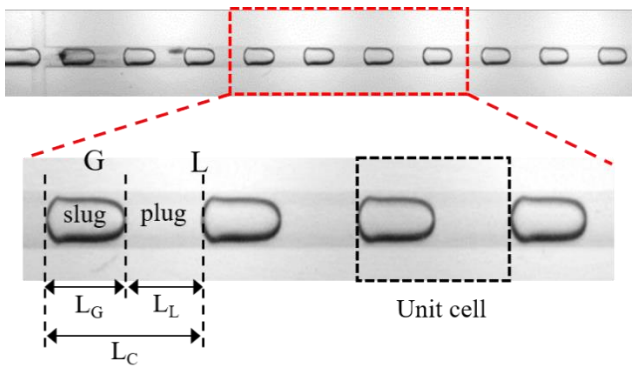

Figure 2-5 Schematic diagram of unit cell.

As for most of the studies, the actual parameter to be monitored is the length of bubble [17, 18]. To a first approximation, bubble volume is calculated by multiplying the cross-section area of microchannel and length of bubble L_G. To increase precision, some researchers have considered the rear and cap of the bubble as two hemispheres. The film of the body is still assumed to be uniform, which indicates a constant cross-section area of the bubble body. In other word, bubble body is considered as a cylindrical shape. The volumes of the rear and cap are calculated by the formula for the volume of a sphere. The volume of the body is calculated by multiplying the cross-section area of the body by the body length [19, 20]. This technique is, therefore, effectively limited to the bubbles with a bilateral (cap-to-rear) symmetrical shape as shown in Figure 2-6 (a,b). However, with the increase of superficial liquid velocity j_L, bubbles become bullet-shaped gradually. Bubble cap becomes pointed and the rear becomes flat as shown in Figure 2-6 (c-e). They are completely bilateral asymmetrical, and the width of the body film δ varies along the body length [21, 22]. The above assumptions for simplicity

are not valid anymore for deformed bubbles. Consequently, the 3D bubble reconstruction and new bubble volume calculation method are necessary to develop to estimate the mass transfer coefficient.

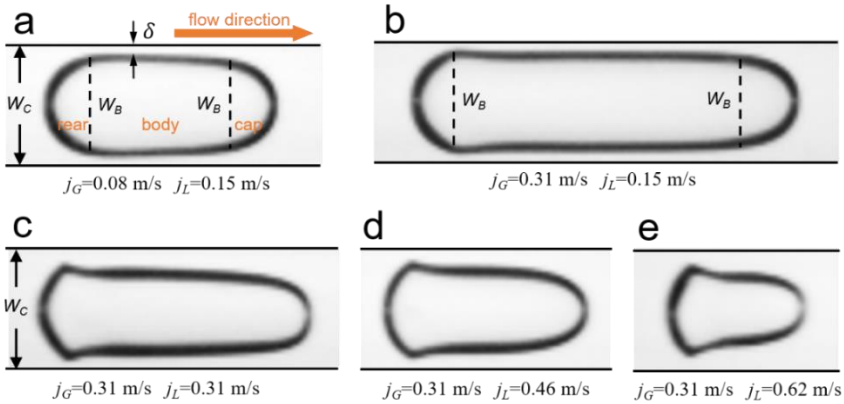

Figure 2-6 (a-b) symmetric bubbles; (c-d) deformed bubbles.

Micro laser-induced fluorescence (micro-LIF) is an advanced technology to obtain the concentration distribution in liquid plugs [23, 24]. But due to the limitation of equipment, LIF was not used in this thesis. Although this thesis only focuses on the experimental method, CFD is a useful tool to obtain information that cannot be obtained from experiments [15]. Verification between numerical and experimental results can enhance the reliability of conclusion. Therefore, micro-LIF and CFD will be considered as a part of my future work.

2.2 Porous media with microchannel network

Porous media is a network of microchannels formed by interconnected pores, which widely exists in industrial and subsurface applications. Fluids can flow through or trap in the pore space. When two fluids flow in porous media, the interface between fluids may become unstable. Such instability will limit extraction effectiveness and cause leakage in the applications.

2.2.1 Interfacial instability

The interface will become unstable when a more viscous fluid is displaced by a less viscous fluid, and thus fingering pattern will occur [25]. Although the first scientific study was conducted by Hill (1952) [26], the interfacial instability is called Saffman-Taylor instability[27] due to Saffman and Taylor's now-classical work in 1958 about essentially identical liner-instability analyses of one-dimensional displacement [27]. Since then, this beautiful physical phenomenon has attracted extensive attention. Various configurations have

been used to investigate this phenomenon. In the rectangular configuration, the pattern will evolve until a single stable finger is generated (Figure 2-7(a)). In the radial configuration, fingering will spread and split up successively (Figure 2-7(b)). This instability is traditionally investigated in a very thin space between two closely spaced parallel glass sheets, which is called Hele-Shaw cell. In addition, researcher also fabricated the solid structure like posts in the cell to form a porous space. Zhao et al. [28] studied fluid-fluid displacement in disordered media patterned with vertical posts. The post pattern forms a macroscopically homogeneous porous structure, in which incomplete pore-scale displacement can be observed. The non-compact viscous fingering pattern with branches was generated in the radial direction.

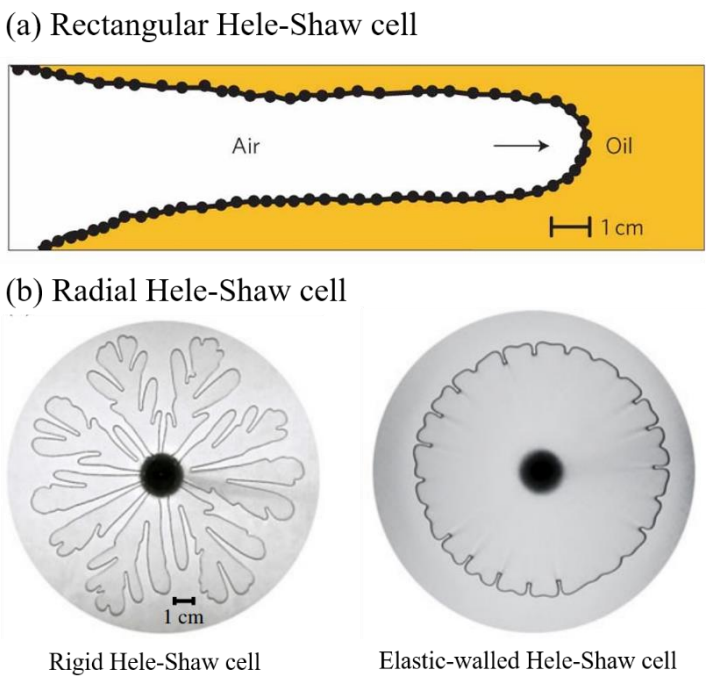

Figure 2-7 Fingering pattern in literature: (a) Hele-Shaw cell with rectangular configuration [29]; (b) Hele-Shaw cell with radial configuration [30]. (Reprint by permission from the publisher)

2.2.2 Phase diagram and displacement pattern in porous media

Apart from the Hele-Shaw cell, the porous structure is also fabricated in porous media chips. The holes are connected to each other, forming microchannel network. Intensive work has been conducted to study the instability dynamics at core scale [31] and macroscale [32]. In addition, microscale is also an interesting topic of research. In porous media chips with microscale structures, related dynamic capillary pressure, relaxation time [33] and transient flow states [34] play a significant role in the fingering displacement process. Depending on

the wettability of invading phase and defending phase, the displacement process is divided into two types: drainage and imbibition. When non-wetting fluids displaces wetting fluids, this process is called drainage. The imbibition process is the opposite. Viscous force, surface tension and capillary force mainly control the flow motion, which can be characterized by two dimensionless numbers: the capillary number *Ca* and the viscosity ratio *M* of the invading phase to the defending phase.

$$Ca = \frac{\mu_i u_i}{\sigma_d} \tag{2-5}$$

$$M = \frac{\mu_i}{\mu_d} \tag{2-6}$$

Where, μ_i and μ_d denote dynamic viscosity of the invading and defending phases, respectively. u_i is Darcy velocity of the invading phase, and σ_d is the surface tension of dispersed phase. As shown in Figure 2-8, the phase diagram of fingering displacement was mapped based on the dimensionless numbers $Log_{10}Ca$ and $Log_{10}M$. The morphologies of the fingering pattern in different regimes are illustrated, including viscous fingering (VF), capillary fingering (CF), crossover zone (CZ) and stable displacement (SD) [35, 36].

- Viscous fingering (VF). In the region with lower $Log_{10}M$ and high $Log_{10}Ca$, a narrow finger pattern with branches is observed because the viscous force mainly controls the process. At the moment when the cap of the finger reaches the outlet, called breakthrough, the displaced area is the lowest.
- Capillary fingering (CF). At high viscosity ratio and low capillary number, the finger pattern becomes wide and the number of branches reduces. Capillary fingering is mainly controlled by capillary force.
- Crossover zone (CZ). The width of the finger is between that in CF and VF regimes, because displacement is controlled by the viscous force and capillary force simultaneously.
- Stable displacement (SD). When the viscosity ratio and capillary number are both high, the interface keeps stable and the displaced area is the highest at the breakthrough moment.

Many studies have been conducted to explore fingering pattern transition and the boundaries to distinguish different regimes, which provides guidance for the prediction of flow patterns. By deriving a simple force balance relating viscous to capillary forces, Lenormand et al.[37] firstly proposed the boundaries to distinguish different flow regimes in a pore network as shown in blue solid lines of Figure 2-8. The result was obtained by experiment and simulation, but position of the boundaries is system-dependent. The now-famous boundaries (green dot lines) were defined by Zhang et al.[38] based on an almost homogeneous and isotropic micromodel. It is unlike for the multiple flow regime to coexist, so the area of crossover zone is narrower than that defined by Lenormand et al.[37]. Recently, Guo et al.[39] also proposed the boundaries on the base of the drainage process in the pore network that represents the pore distribution of Berea sandstone. As shown in red dash lines of Figure 2-8, the boundaries are completely inconsistent with that of Zhang et al.[38]. The crossover zone between the CF and

VF is extremely narrow. The reason may originate from pore size distribution and domain size.

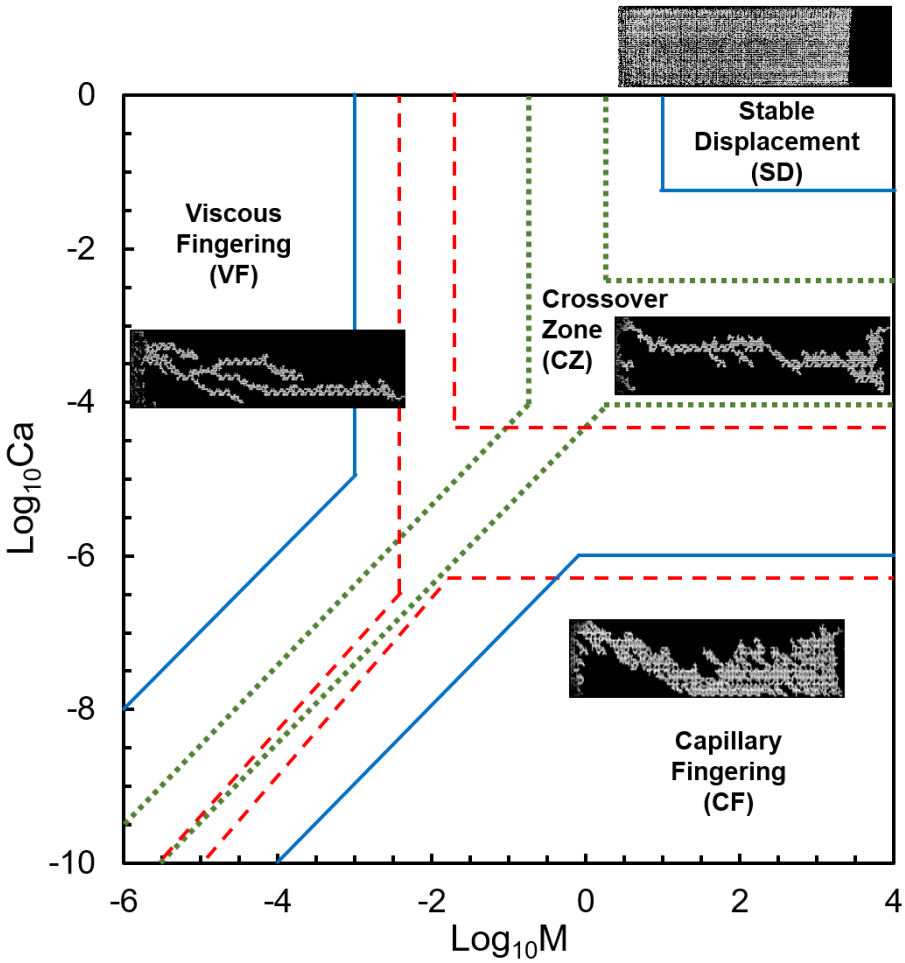

Figure 2-8 Phase diagram of fingering displacement (blue solid lines, green dot lines and red dash lines are the boundaries between different displacement patterns defined by Lenormand et al.[37], Zhang et al.[38] and Guo et al.[39], respectively.).

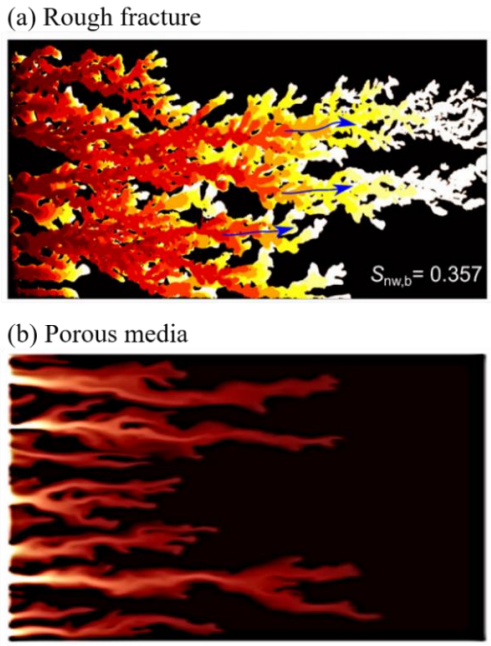

Figure 2-9 Fingering pattern in rough fracture [40] and porous media [41]. (Reprint by permission from the publisher)

As mentioned above, fingering displacement in porous media is greatly important in many subsurface and industrial applications. However, this non-compact fingering pattern resulting from interfacial instability has an important influence on extraction effectiveness and leakage risk, which are related to economic benefits and storage safety. Therefore, extensive work focused on the dynamic evolution process of fingering pattern in rough fracture and porous media as shown in Figure 2-9. In addition to experiments, lattice Boltzmann method (LBM) [42, 43] was used to simulate the complex fingering displacement and explore the mechanisms of interfacial instability. The fingering pattern was quantified by parameters such as cap velocity [44], finger width [45], number of fingers [46], interface curvature [47-49], breakthrough time [44, 46], invading area [50] and saturation [46, 51], fractal dimension [45, 52], and pressure difference [51, 53]. Most research was limited to the displacement process before or at the breakthrough moment. However, evolution of fingering patterns after breakthrough is still of great importance. It can provide guidance on how to achieve relatedly high extraction efficiency in the shortest time and avoid leakage. The mathematical model based on non-equilibrium effects was created [54, 55] and gradually modified [56-58] to describe two-phase displacement process. After breakthrough, the evolution of displacement pattern varies in different flow patterns. When the displaced area becomes maximum, steady state reaches. Yet, the evolution process from breakthrough to steady state remains unclear. In different flow regimes, the dynamical transition of fingering patterns from breakthrough to steady state and the underlying mechanisms still need to be explored further [45].

CHAPTER 3

Experimental setups and methods

In this chapter, the microfluidics platform and experiment procedure are presented. Besides, the geometry of microchip (microchannel and porous media), 3D bubble reconstruction and bubble volume calculation, image processing method and data processing procedure are introduced.

3.1 Geometry of microchips

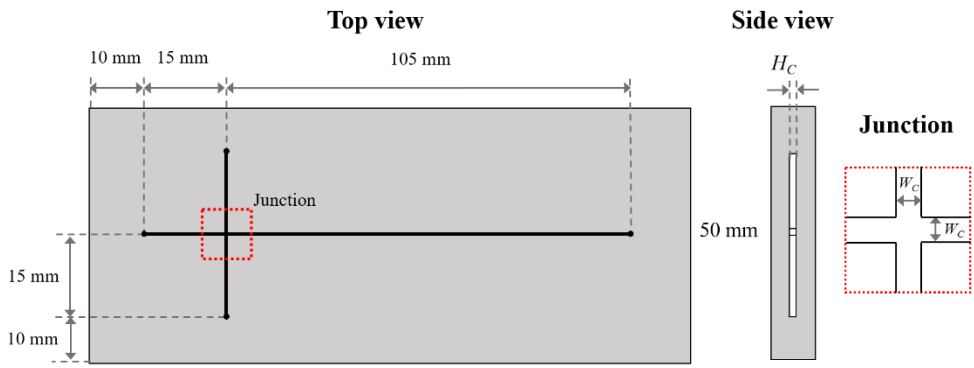

	Width W_C	Depth H_C
Square	600 μm	600 μm
Rectangular	600 μm	300 μm

Figure 3-1 Geometrical details of the rectangular and square microchannel.

Figure 3-1 indicates the geometry of two microchannels with square and rectangular cross-sections, manufactured by Little Things Factory, Germany. A cross-shaped junction downstream of the inlets merges the flows from the three inlets. After the junction, a straight main microchannel with 105 mm length is connected. As for square microchannel, the width

and depth are both 600 μm. As for rectangular microchannel, the width and depth are 600 μm and 300 μm. The accuracy of the width and depth is within ±10 μm. The material of chip is glass, so it is intrinsically hydrophilic for water.

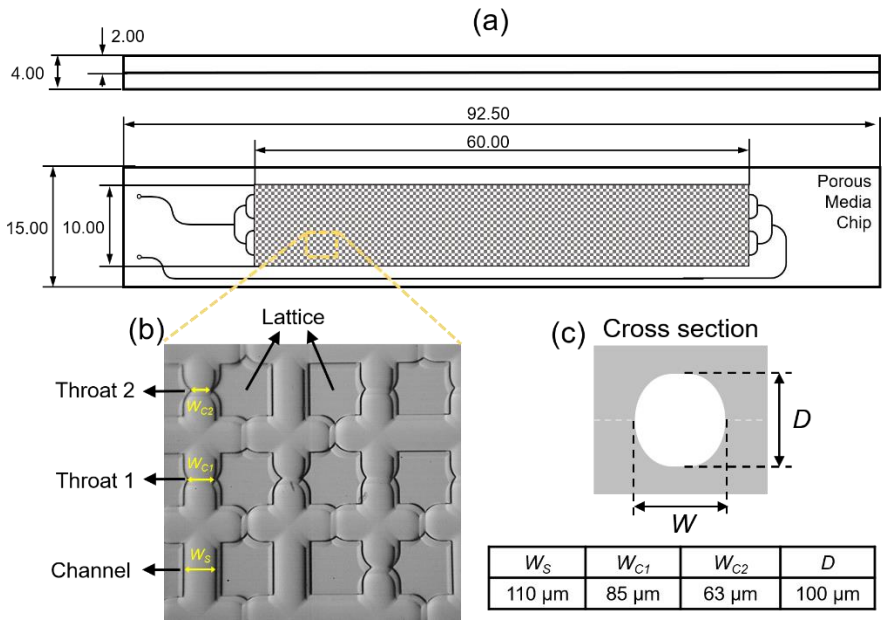

W_S	W_{C1}	W_{C2}	D
110 μm	85 μm	63 μm	100 μm

Figure 3-2 Details of porous patterned microfluidic chip: (a) chip dimensions with mm unit; (b) geometries of porous patterns inside the chip; (c) cross section of the channel.

Figure 3-2 shows the geometry of the porous media chip with microchannel network, manufactured at Dolomite company. The porous media chip involves a gas inlet and liquid outlet and a 60×10 mm porous domain. The gas inlet and liquid outlet are designed as a tree-shaped layout, which can ensure a uniform inflow and outflow. Figure 3-2 (b) shows the micrograph of the porous domain. The microchannel network is formed by the orderly arrangement of the different lattices. There are straight channels and two types of throats with the width 110 μm, 85 μm and 63 μm, respectively. Figure 3-2 (c) indicates the cross-section of channels with the same depth D 100 μm. The material is quartz glass with 5 nm surface roughness (Ra). Its measured contact angle is 38.3° for water, so it is hydrophilic. The channel of the chip is fabricated by the etching process, which will further reduce the contact angle. The contact angle measurements experiment (see the last row of Table 3-5) found that glycerol has a similar static contact angle as the water.

3.2 Experimental setup and Experimental procedure

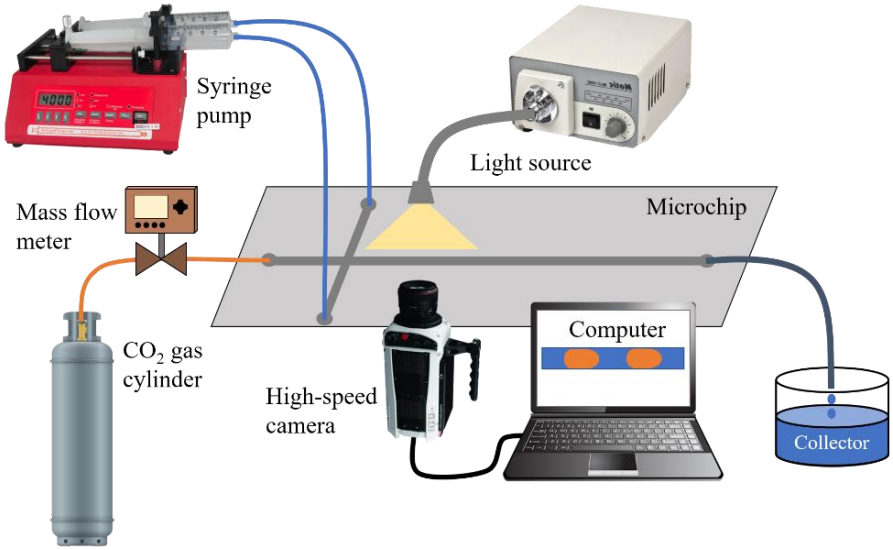

Figure 3-3 Experimental setup for single microchannel.

Microfluidics platform was built up to explore gas-liquid flow and mass transfer in microchannels. As shown in Figure 3-3, the experimental setup consists of fluid feeding system, horizontally placed microchannel, high-speed imaging system and residue liquid collector. The liquid (deionized water) was injected into the two side inlets, controlled by the syringe pump (New Era NE-4000). The CO_2 gas was introduced into the center inlet, controlled by the gas mass flow meter (Bronkhorst EL-Flow prestige FG-200CV). Gas and liquid merged at the junction and then the gas-liquid flow is generated in the main microchannel. A high-speed camera (Phantom V611, maximum 6242 fps at full resolution 1280 × 800) equipped with a lens (micro-NIKKOR 105mm) was used to capture the images and videos of the gas-liquid flow. Light source provided powerful cold light (Motic, MLC-150C) to increase the brightness for photography. The reduced recording resolution (1280 × 104) was selected to increase the recording speed to 20000 fps at a 20 μs exposure time. By counting the number of pixels across the channel width, the spatial resolution was measured and was 19.6 μm/pixel. Computer was connected to the camera to record the data. The collector was used to collect the residue water.

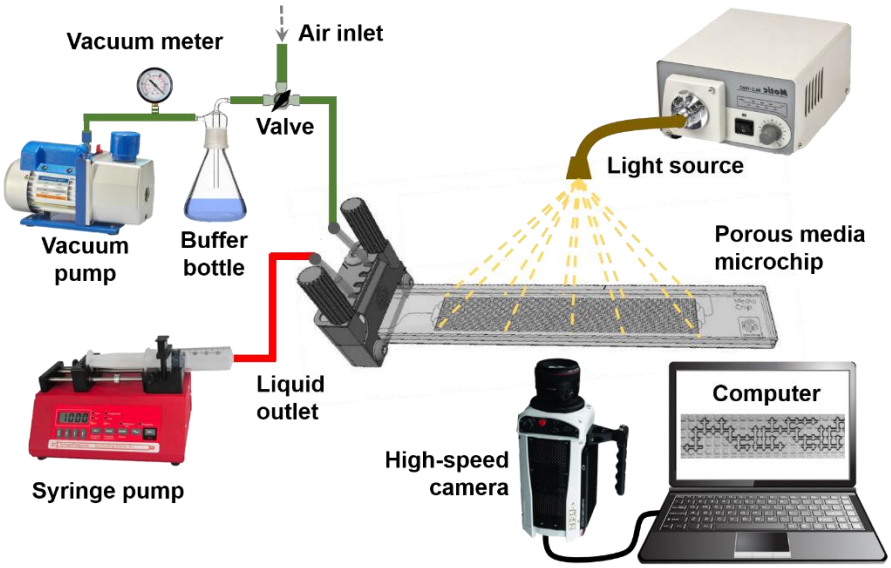

Figure 3-4 Experimental setup for gas-liquid displacement in porous media.

Figure 3-4 presents the experimental setup for gas-liquid displacement in porous media. Prior to the experiment the whole porous medium should be filed with liquid. To achieve this, the vacuum pump was used to extract the air from the pore space until in the pressure indicated by the vacuum meter was close to 10^{-2} bar. Thereafter, the liquid was injected into the pore space at a low flow rate (about 20 mL/h). In a near-vacuum state, the liquid can easily fill the porous spaces without any trapped bubbles. The gas-liquid displacement started when the air was injected into porous domain from the gas inlet by using the syringe pump to suck the liquid at the desired flow rate in the reverse direction. The high-speed camera was used to capture the images and videos of gas-liquid fingering displacement process in porous domain at a 20μs exposure time. A cold light source provided the illumination. In order to record the whole fingering displacement, a 1280 × 256 recording window at a rate between 24 and 2000 fps with a 47.62 μm/pixel spatial resolution was performed on the whole porous domain. In addition, in order to capture the local dynamical behavior of displacement, a macro lens (NAVITAR-12X) was used to record the reduced visualization window of 242 × 592 at 6000 fps and spatial resolution of 9.0 μm/pixel. A computer was connected to the camera to collect the data.

3.3 Image processing method and data processing procedure in microchannel

3.3.1 Image processing method of bubble in microchannel

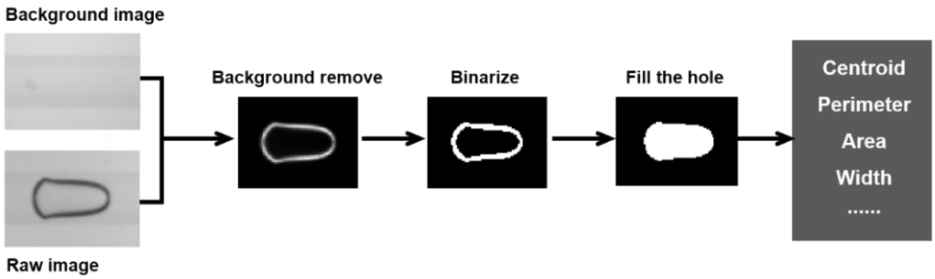

Figure 3-5 Image processing procedure for bubble in microchannels.

Since the images were recorded in a high-speed mode, several thousands of frames were available to provide details of the process of bubbles flowing through the channel. These images can be processed in batches by developed in-house MATLAB code. The image process procedure was shown in Figure 3-5. Firstly, liquid was injected into microchannel without the gas phase. About 1000 frames of background images were captured in this condition. The background image was generated by averaging the gray levels of each pixel of these images. Then all the raw images of the case were divided by the background image pixel by pixel to remove the background. In the processed images, the gray level of the pixel in the center of the bubble and the outer region is close to 1. But that within the boundary of the bubble is much higher than 1. By setting threshold value 1.2, the images were binarized. After filling the holes of inner area of bubble, the binarized bubble shape was obtained. Based on binarized bubble shape, bubble characteristics, such as the centroid, perimeter, area, width, etc., were measured by MATLAB algorithm. The velocity of the bubble j_B was obtained by fitting the position of the centroid of the bubble over time. Finally, the bubble volume V_B and interfacial area between gas and liquid phase A_B were calculated, which will be detailed in the following subsection.

3.3.2 Calculation of bubble 3D volume V_B and interfacial area A_B in rectangular microchannel based on 2D projection

The image of 3D bubble captured by camera is a 2D projection. But the bubble volume and interface area should be determined in 3D. It is necessary to converse 2D projection to 3D volume. The theoretical model based on the principle of interfacial energy minimization is implemented for the conversion[59]:

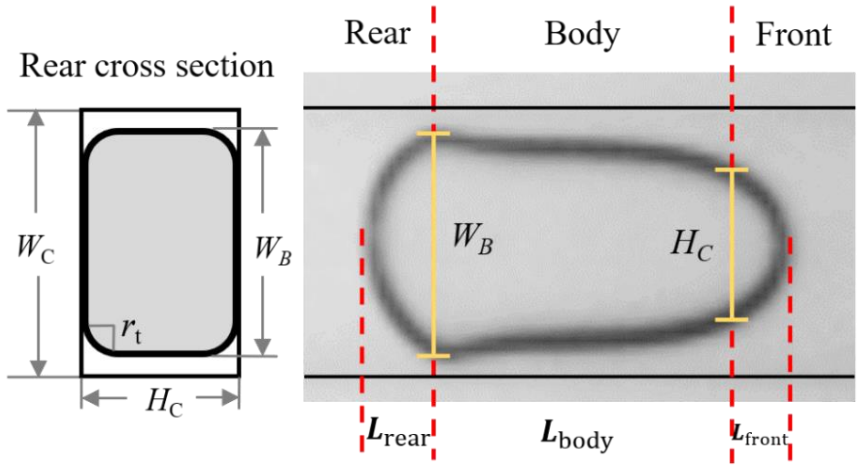

Figure 3-6 Schematic diagram of bubble (The front of bubble is divided at the position where the width is smaller than H_C ($300\ \mu m$)).

As shown in Figure 3-6, the cross section is characterized by width W_B, depth H_B and curvature radius r_t at the channel corner. According to the model, the curvature radius r_t, the cross-sectional area A_{bd} and the perimeter P_{bd} are calculated by:

$$r_t = \frac{H_B + W_B - \sqrt{{H_B}^2 + (\pi - 2)H_B W_B + {W_B}^2}}{4 - \pi} \approx \left(\frac{2}{H_B} + \frac{2}{W_B}\right)^{-1} \tag{3-1}$$

$$A_{bd} = H_B W_B - (4 - \pi){r_t}^2 \tag{3-2}$$

$$P_{bd} = 2(H_B + W_B - 4r_t + \pi r_t) \tag{3-3}$$

The length of the bubble rear is assumed as $L_{rear} = W_B/2$. The film in the depth side is negligible, which means $H_B = H_C$. As shown in Figure 3-6, bubble is divided into three parts: rear cap, front cap and body, and the volumes of these are calculated separately, as is described below.

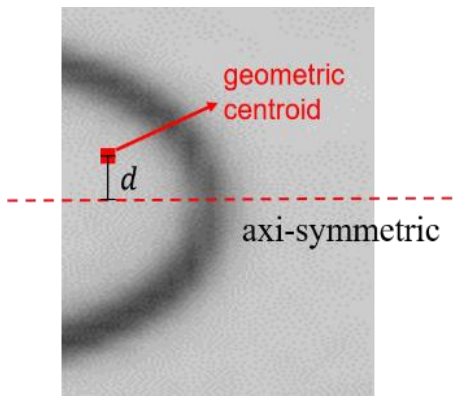

Figure 3-7 Schematic diagram of the front cap.

As for the front cap (Figure 3-7), the width is smaller than H_C ($300\ \mu m$) and it can therefore be considered as a revolution body [60]. The volume and interface area are then calculated based on the Pappus theorem:

$$V_{front} = S_{front} \times 2\pi d \tag{3-4}$$

$$A_{front} = L_{boundary} \times 2\pi d \tag{3-5}$$

Here, d is the distance between the centroid of the upper front cap and the revolution axis. S_{front} is the projected area of the upper front cap. $L_{boundary}$ is the length of the boundary of the upper front cap.

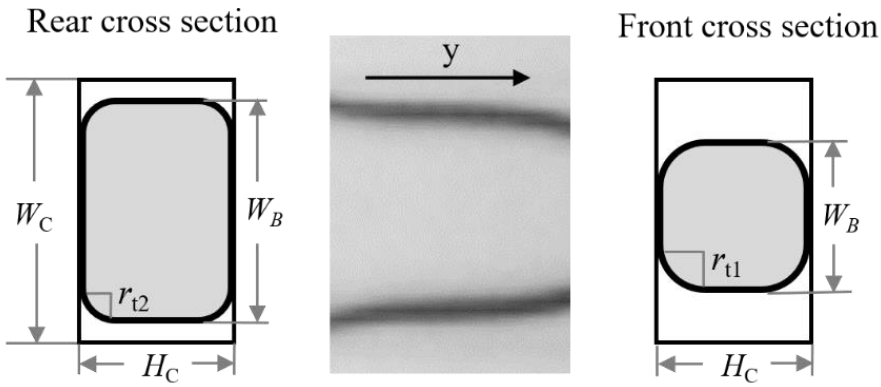

Figure 3-8 Schematic diagram of body.

For the body part (Figure 3-8), It is assumed that the cross-section area $A_b(y)$ and the perimeter $P_b(y)$ decrease linearly from rear to front, and these are calculated as:

$$A_b(y) = \frac{A_{bd1} - A_{bd2}}{L_{body}} y + A_{bd2} \tag{3-6}$$

$$P_b(y) = \frac{P_{bd1} - P_{bd2}}{L_{body}} y + P_{bd2} \tag{3-7}$$

Based on Eq. (3-6) and Eq. (3-7), and the cross-section area A_{bd1}, A_{bd2} and perimeter P_{bd1}, P_{bd2} for the front cap side and rear cap side are calculated. Therefore, the volume and interface area of the body can be measured as the integrals:

$$V_{body} = \int_0^{L_{body}} A_b(y)\, dy = \frac{1}{2} L_{body}(A_{bd1} + A_{bd2}) \tag{3-8}$$

$$A_{body} = \int_0^{L_{body}} P_b(y)\, dy = \frac{1}{2} L_{body}(P_{bd1} + P_{bd2}) \tag{3-9}$$

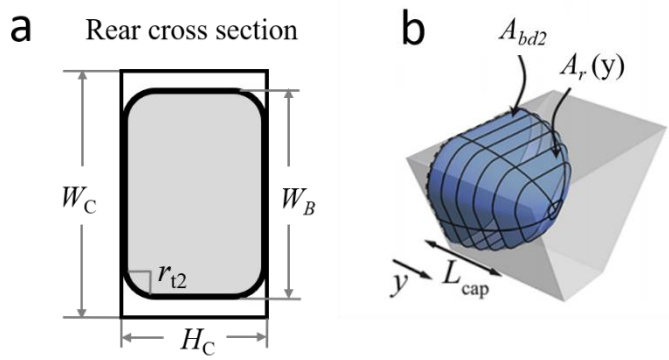

Figure 3-9 Schematic diagram of rear cap: (a) rear cross section; (b) shape of the cap [59] (Reprint by permission from the publisher).

As for the rear cap (Figure 3-9), it is assumed that the cross-section area $A_r(y)$ decreases monotonically from $A_r(y) = A_{bd2}$ at $y = 0$ to $A_r(y) = 0$ at $y = L_{rear}$. Similarly, the perimeter monotonically decreases from $P_r(y) = P_{bd2}$ at $y = 0$ to $P_r(y) = 0$ at $y = L_{rear}$ [59].

$$A_r(y) = A_{bd2}\left(1 - \frac{y^2}{{L_{rear}}^2}\right) \tag{3-10}$$

$$P_r(y) = P_{bd2}\left(1 - \frac{y^2}{{L_{rear}}^2}\right) \tag{3-11}$$

So, the volume V_{rear} and interface area A_{rear} of the rear cap can be calculated as:

$$V_{rear} = \int_0^{L_{rear}} A_r(y)\, dy = \frac{2}{3} L_{rear} A_{bd2} \tag{3-12}$$

$$A_{rear} = \int_0^{L_{rear}} P_r(y)\, dy = \frac{2}{3} L_{rear} P_{bd2} \tag{3-13}$$

The volume and cross-section area of the bubble can be measured by sum:

$$V_B = V_{rear} + V_{body} + V_{front} \tag{3-14}$$

$$A_B = A_{rear} + A_{body} + A_{front} \tag{3-15}$$

A mass centroid is obtained based on the calculated bubble volume, which is distinct from the 2D image centroid. Then bubble velocity is obtained by fitting the position of mass centroid with time.

3.3.3 3D reconstruction of bubble in square microchannel based on slicing method

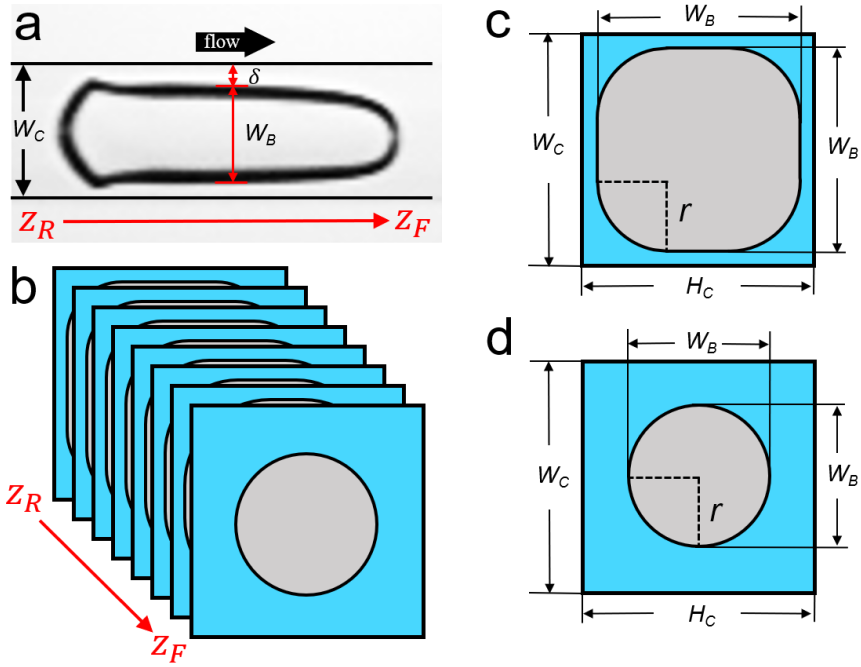

Figure 3-10 Physical image captured by the high-speed camera; (b) Schematic diagram of bubble slices from bubble rear z_R to bubble front z_F; (c) Schematic diagram of cross-section of the slice when $W_B(z_B) > 2r$; (d) Schematic diagram of cross-section of the slice when $W_B(z_B) = 2r$.

Based on the slicing method [61], the 3D shape of symmetric bubbles and deformed bubbles in square microchannel were reconstructed. As shown in Figure 3-10 (a, b), the bubble was sliced along the streamwise direction z_B according to the pixels. $W_B(z_B)$ was estimated by in-house codes of MATLAB at each slice. When bubbles flow in a square microchannel, the corner flow and liquid film flow between bubble surface and wall will occur. According to the principle of interfacial energy minimization [59], the cross-section of a slice is assumed to involve a square and four circular arcs with the radius r at the corners when width of bubble $W_B(z_B) > 2r$, as shown in Figure 3-10 (c). When the gas/liquid interface contacts the walls of microchannel, the width of body film δ is equal to zero. The stress boundary condition at the interface can be simplified to $\nabla \cdot \mathbf{n} = \frac{1}{r}$ [62], where $\mathbf{n}$ is the unit vector normal to the interface in the outward direction. After integrating and using the Gauss theorem, r can be calculated by the ratio of the area and perimeter of cross-section of microchannel:

$$r = \frac{A_C}{P_C} = \frac{{W_C}^2 + (\pi - 4)r^2}{4W_C + (2\pi - 8)r} \tag{3-16}$$

Here, P_C and A_C are the cross-section perimeter and cross-section area when the width of body film δ is equal to zero. The width of channel $W_C = 600$ μm. So, r is calculated as 159 μm according to Eq. (3-16). When $W_B(z_B) \geq 2r$, the width of bubble $W_B(z_B)$ varies but r doesn't change, because r only depends on the channel aspect ratio. When the slice is located near bubble front or rear, W_B reduces. When $W_B(z_B) = 2r$, the cross-section becomes a circle with the diameter W_B as shown in Figure 3-10 (d). When $W_B(z_B) < 2r$, the diameter W_B of circle becomes smaller as the slice further closes to bubble front or rear. Therefore, the cross-sectional area $A(z_B)$ and the interfacial perimeter $P(z_B)$ of the bubble slices at each z_B position can be calculated as:

$$A(z_B) = \begin{cases} W_B^2(z_B) + (\pi - 4)r^2, & W_B(z_B) > 2r \\ \frac{\pi}{4} W_B^2(z_B), & W_B(z_B) \leq 2r \end{cases} \tag{3-17}$$

$$P(z_B) = \begin{cases} 4W_B(z_B) + (2\pi - 8)r, & W_B(z_B) > 2r \\ \pi W_B(z_B), & W_B(z_B) \leq 2r \end{cases} \tag{3-18}$$

The volume V_B and interfacial area A_B of bubble are calculated by superimposing all slices N_z:

$$V_B = \int_{z_R}^{z_F} A(z_B) dz_B \approx \Delta z \sum_{i=1}^{N_z} A(z_{B,i}) \tag{3-19}$$

$$A_B = \int_{z_R}^{z_F} P(z_B) dz_B \approx \Delta z \sum_{i=1}^{N_z} P(z_{B,i}) \tag{3-20}$$

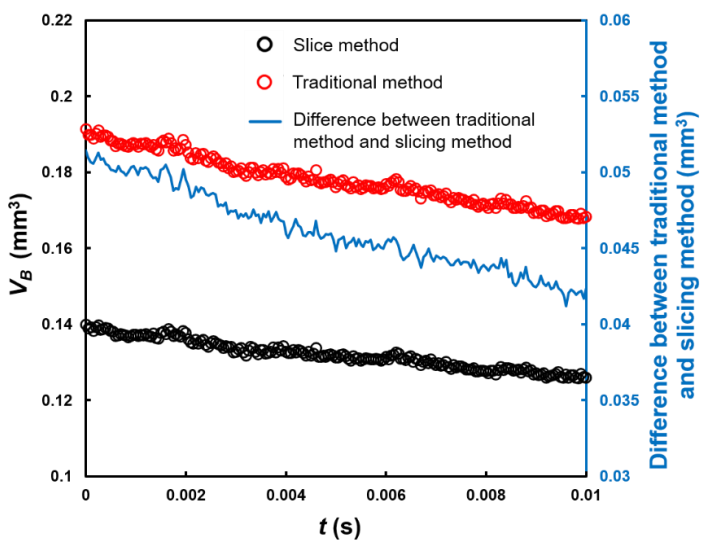

Figure 3-11 Comparison between the traditional method and the slicing method.

In the traditional method, the rear and cap of the bubble are considered as two hemispheres. The volume is calculated by volume formula of sphere. Besides, the width of bubble body W_B is assumed to be constant. Therefore, traditional bubble volume calculation is as below:

$$(V_B)_{tra} = \left[\overline{W_B}^2 + (\pi - 4)r^2\right]\left(L_B - \overline{W_B}\right) + \frac{1}{6}\pi\overline{W_B}^3 \quad (3\text{-}21)$$

Here, L_B is the length of bubble. Because of the varying width of deformed bubble body, an average value $\overline{W_B}$ was used. Figure 3-11 confirms that the bubble volume is overestimated by using the traditional method. The volume difference between the traditional method and the slicing method is from 0.0185 to 0.043 mm^3, which is approximately 35% of V_B obtained by the slicing method. So, the slicing method is more feasible to estimate the volume of the deformed bubble.

3.3.4 Principle of mass transfer coefficient calculation

As mentioned above, the mass transfer coefficient of CO_2 bubbles can be calculated by using the two-film theory and ideal gas law:

$$k_L = -\frac{1}{RTA_B(C_{L,i}-C_{L,b})}\frac{d(P_{CO_2}V_{CO_2})}{dt} = -\frac{1}{RTA_B(C_{L,i}-C_{L,b})}\left(P_{CO_2}\frac{dV_{CO_2}}{dt} + V_{CO_2}\frac{dP_{CO_2}}{dt}\right) \quad (3\text{-}22)$$

Here, $\frac{dP_{CO_2}}{dt}$ of CO_2 bubbles is difficult to measured. To measure it, N_2 was used to repeat all the cases of CO_2 experiments. Due to N_2 has no mass transfer with water, we can have:

$$\frac{d(P_{N_2}V_{N_2})}{dt} = V_{N_2}\frac{dP_{N_2}}{dt} + P_{N_2}\frac{dV_{N_2}}{dt} = \frac{dM_{N_2}}{dt}RT = 0 \quad (3\text{-}23)$$

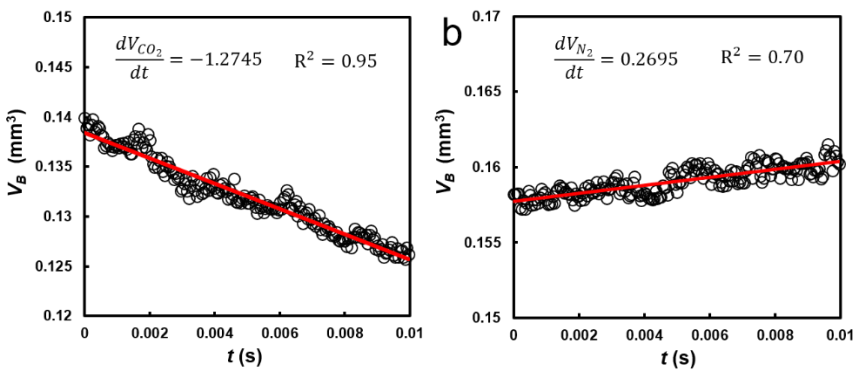

Figure 3-12 (a) Volume changes of a CO_2 bubble with time and the fitting curve; (b) Volume changes of a N_2 bubble with time and the fitting curve.

Based on the bubble volume calculation method above, the volumes of CO_2 and N_2 bubbles V_{CO_2} and V_{N_2} can be measured. Figure 3-12 shows the volume change of CO_2 and N_2 bubbles flowing through the microchannel at the same case (same gas and liquid volume flow rate).

The CO_2 bubble volume decreased over time due to the mass transfer from bubble to liquid, while N_2 bubble volume over time due to pressure drop. Actually, the volume of CO_2 also expands because of pressure drop, but it is offset by the volume reduction caused by mass transfer. As show in Figure 3-12, the initial volumes of CO_2 and N_2 bubbles are close, because the gas injection volume controlled by flow meter are same at the same case. Therefore, $\frac{V_{CO_2}}{V_{N_2}}$ is approximately 1. By ignoring the effect of bubble volume change on pressure drop, the pressure drops of CO_2 and N_2 bubbles flowing through microchannels are identical at same flow rate, which is equal to:

$$\Delta P = P - P_{atmosphere} \tag{3-24}$$

Therefore, the pressure in microchannel P is also same as for CO_2 and N_2 bubbles, which means $\frac{dP_{N_2}}{dt} = \frac{dP_{CO_2}}{dt}$ and $\frac{P_{N_2}}{P_{CO_2}} = 1$. Eq. (3-23) is substituted into Eq. (3-22):

$$k_L = -\frac{P_{CO_2}}{RTA_B(C_{L,i}-C_{L,b})}\left(\frac{dV_{CO_2}}{dt} - \frac{dV_{N_2}}{dt}\right) \tag{3-25}$$

According to ideal gas law, the volume expansion of bubbles resulting from pressure drop is independent of gas species. Therefore, it is reasonable to use N_2 volume expansion to correct the CO_2 volume expansion result from pressure drop. $\left(\frac{dV_{CO_2}}{dt} - \frac{dV_{N_2}}{dt}\right)$ represents the volume reduction purely resulting from mass transfer.

Because the mass transfer rate of CO_2 is relatively low, the concentration at the bulk $C_{L,b}$ is much lower compared with the concentration at the interface $C_{L,i}$. So, $C_{L,b}$ can be neglected. Henry's law describes the solubility of gases absorbed by water:

$$\frac{H}{RT} = \frac{C_{L,i}}{P_{CO_2}} \tag{3-26}$$

Here, H is the Henry constant in dimensionless form, which is 0.827 for CO_2 at 298 K [63]. Substituting the Eq. (3-26) into Eq. (3-25), the mass transfer coefficient k_L can be calculated as:

$$k_L = -\frac{1}{A_B H}\left(\frac{dV_{CO_2}}{dt} - \frac{dV_{N_2}}{dt}\right) \tag{3-27}$$

After linear fitting, $\frac{dV_{CO_2}}{dt}$ and $\frac{dV_{N_2}}{dt}$ can be obtained as shown in Figure 3-12. Based on the above calculation method of the interfacial area A_B of CO_2 bubble, we can obtain mass transfer coefficient k_L finally.

3.4 Image processing method of fingering pattern in porous media

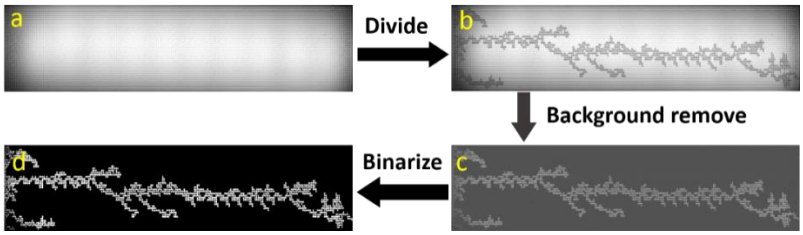

Figure 3-13 Procedures of image processing of fingering pattern in porous media: (a) background image of porous patterns before gas invasion; (b) raw image of gas invasion; (c) greyscale image after subtracting background; (d) binarized image.

Image processing procedures of fingering pattern in porous media is similar to the procedure for bubble in single microchannel. The procedure was achieved by an in-house code in MATLAB. As shown in Figure 3-13 (a), about 1000 frames of background images were captured to average the gray value pixel by pixel. Then, all the raw images of cases were divided by the average background image to remove the background as shown in Figure 3-13 (c). Finally, the processed image was binarized by setting the 1.2 threshold value as shown in Figure 3-13 (d). Popular algorithms, such as box-counting, were used to measure the invading velocity, invading area and fractal dimension.

3.5 Dimensionless numbers and Experimental conditions

This chapter presents the experimental conditions of each paper. Due to its universality, dimensionless numbers can expand the physical phenomena of research to other scalable systems with different sizes. Therefore, dimensionless numbers, including Reynolds number, Capillary number, Sherwood number and Schmidt number, were calculated based on these operating parameters and presented in this chapter.

Paper i (rectangular microchannel):

As for the research on rectangular microchannel, the dispersed phase is CO_2 and the continuous phase is de-ionized water. The physical properties at 20.5 ± 0.5 °C of them are listed in Table 3-1.

Table 3-1 Physical properties at 20.5 ± 0.5 °C

Property		Unit	water	CO_2
Density	ρ	kg/m^3	998.2	1.797
Viscosity	μ	10^{-6} Pa · s	1005	15
Surface tension	σ	N/m	0.0728	-
Diffusivity	D_{dif}	10^{-9} m^2/s	1.954	-

The experiments were carried out with varied gas flow rates and liquid flow rates. The liquid flow rate varied from 5 to 700 mL/h, and the gas flow rate varied from 50 to 2000 mL/h. Dimensionless numbers in slug flow regime, including Reynolds number, Capillary number and Sherwood number, are listed in Table 3-2.

Table 3-2 Dimensionless number in slug flow regime

Dimensionless number		Value range
Reynolds number of the liquid phase	$Re_L = \frac{D_h j_L \rho_L}{\mu_L}$	30.7 - 306.6
Reynolds number of the gas phase	$Re_G = \frac{D_h j_G \rho_G}{\mu_G}$	3.7 - 73.9
Reynolds number in a cell	$Re_T = \frac{D_h j_T \rho_L}{\mu_L}$	611.6 - 924.1
Capillary number of the gas phase	$Ca_B = \frac{\mu_L j_B}{\sigma_L}$	0.0028 - 0.024
Sherwood number	$Sh = \frac{k_L D_h}{D_{dif}}$	84.9 - 1017.3

Paper ii (square microchannel):

As for the research on square microchannel, the dispersed phase is CO_2 and N_2 and the continuous phase is de-ionized water. The physical properties at 20.5 ± 0.5 °C of them are shown in Table 3-3.

Table 3-3 Physical properties at 20.5 ± 0.5 ◦C

			water	CO_2	N_2
Density	ρ	kg/m^3	998.2	1.797	1.138
Viscosity	μ	mPa·s	1.005	0.0150	0.0179
Surface tension	σ	N/m	0.0728	/	/
Diffusion coefficient	D_{dif}	10^{-9} m^2/s	1.954	/	/

The experiments were carried out with varied gas flow rates and liquid flow rates. The liquid flow rate varied from 2 to 1400 mL/h, and the gas flow rate varied from 100 to 2000 mL/h. Dimensionless numbers in slug flow regime, including Reynolds number, Schmidt number, Capillary number and Sherwood number, are listed in Table 3-4.

Table 3-4 Dimensionless numbers in slug flow regime

Dimensionless number		Value range
Reynolds number of bubble	$Re_B = \frac{\rho_G j_B D_H}{\mu_G}$	23 - 153
Reynolds number of gas phase	$Re_G = \frac{\rho_G j_G D_H}{\mu_G}$	6 - 66
Reynolds number of liquid phase	$Re_L = \frac{\rho_L j_L D_H}{\mu_L}$	92 - 460
Schmidt number of liquid phase	$Sc_L = \frac{\mu_L}{\rho_L D_{dif}}$	515
Capillary number of both phases	$Ca_T = \frac{\mu_L j_T}{\sigma}$	0.0032 - 0.0234
Sherwood number	$Sh = \frac{k_L D_h}{D_{dif}}$	167 - 1149

Paper iii (porous media):

As for the research on porous media, the mixtures of deionized water and glycerol solution with concentrations varying from 0 - 80%, were used as the defending phase. The air was used as invading phase to displace liquid. Their properties are listed in Table 3-5.

Table 3-5 Physical properties at 20.5 ± 0.5 °C ("Gly" represents glycerol solution)

		Defending phase				Invading phase
		water	40% Gly	60% Gly	80% Gly	air
Density, ρ	(kg/m^3)	998.2	1099	1154	1209	1.138
Viscosity, μ	(mPa·s)	1.01	3.72	10.8	60.1	0.0179
Surface tension, σ	(N/m)	0.0728	0.0695	0.0676	0.0653	-
Contact angle, θ	±4 °	38.3°	39.7°	38.4°	39.2°	-

The viscosity ratio M between the invading phase and defending phase was calculated. Based on different concentrations of glycerol solution, Log_{10}M varied from -1.75 to 3.53 as shown in Table 3-6. Capillary number Ca was calculated and Log_{10}Ca varied from -8.17 to -4.17 when the gas flow rate varied from 0.1-1000 mL/h.

Table 3-6 Dimensionless numbers

Gas flow rate (mL/h)	0.1	1	10	100	1000
Capillary number $\mathrm{Log}_{10}\mathrm{Ca} = \mathrm{Log}_{10}\left(\frac{\mu_I U_I}{\sigma_D}\right)$	-8.17	-7.17	-6.17	-5.17	-4.17
Concentration of glycerol solution	water	40%	60%		80%
Viscosity ratio $\mathrm{Log}_{10}\mathrm{M} = \mathrm{Log}_{10}\left(\frac{\mu_I}{\mu_D}\right)$	-1.75	-2.32	-2.78		-3.53

3.6 Uncertainty analysis

Table 3-7 Uncertainties.

Parameters	Uncertainty	Remarks
Thermocouple T	± 0.2 °C	-
Surface roughness Ra	± 2.0%	-
Contact angle	± 5.0 °	-
Bubble width W_B, cell length L_C	± 0.0196 mm (± 1 pixel)	-
Bubble velocity j_B	Max. ± 2%	-
Cross-sectional area $A(z_B)$ in each slice	Max. ± 0.02 mm^2	$\delta A(z_B) = 2W_B\delta W_B$
Interfacial perimeter $P(z_B)$ in each slice	Max. ± 0.08 mm	$\delta P(z_B) = 4\delta W_B$
Bubble volume V_B	Max. ± 0.005 mm^3	$\delta V_B = \left[\Delta z^2 \sum_{i=1}^{N_z} \delta A\left(z_{B,i}\right)^2\right]^{1/2}$
Interfacial area A_B	Max. ± 0.02 mm^2	$\delta A_B = \left[\Delta z^2 \sum_{i=1}^{N_z} \delta P\left(z_{B,i}\right)^2\right]^{1/2}$

Overall mass transfer coefficient k_L	Max. ± 5%	$\frac{\delta k_L}{k_L} = \left[\left(\frac{\delta A_B}{A_B}\right)^2 + \left(\frac{\delta \frac{dV_B}{dt}}{\frac{dV_B}{dt}}\right)^2\right]^{1/2}$
Volume of cell V_C	Max. ± 0.007 mm^3	$\delta V_C = W_C^2 \, \delta L_C$
Specific interfacial area a	Max. ± 1%	$\frac{\delta a}{a} = \left[\left(\frac{\delta A_B}{A_B}\right)^2 + \left(\frac{\delta V_C}{V_C}\right)^2\right]^{1/2}$
Volumetric mass transfer coefficient $k_L a$	Max. ± 5%	$\frac{\delta k_L a}{k_L a} = \left[\left(\frac{\delta k_L}{k_L}\right)^2 + \left(\frac{\delta a}{a}\right)^2\right]^{1/2}$
Velocity of finger cap U_{cap}	Max. ± 2%	-
Breakthrough time T_B	Max. ± 3%	-
Fingering area A	Max. ± 5%	-
Saturations S	Max. ± 5%	$\frac{\delta S}{S} = \frac{\delta A}{A}$
Fractal dimension FD	Max. ± 7%	$\frac{\delta FD}{FD} = \left[\left(\frac{1}{N \ln 10} \frac{\delta N}{\log(N)}\right)^2 + \left(\frac{1}{\Delta \ln 10} \frac{\delta \Delta}{\log(\Delta)}\right)^2\right]^{1/2}$

CHAPTER 4

Results and Discussion

This chapter shows an overview and summary of the most important results and discussion of three papers. It is divided into two sections i.e., mass transfer of gas-liquid flow in single rectangular and square microchannels and gas-liquid displacement in porous media with microchannel network.

4.1 Single straight microchannels

4.1.1 Flow pattern map

Figure 4-1 shows the flow pattern map in square microchannel. By varying the superficial gas and liquid velocity, the flow regime can cover bubbly flow, slug flow and annular flow. The flow pattern map was compared with boundaries defined by Triplett et al.[9], Akbar et al.[10] and Niu et al.[11]. The transition line in this study between slug and annular-slug flow is located at lower superficial gas velocity compared with that obtained by Triplett et al.[9], while it is in great agreement with that of Akbar et al. [10] and Niu et al.[11]. As the same as Niu et al.[11], the present map didn't distinguish the slug-annular and annular flow. The transition line between bubbly and slug flow didn't coincide with that proposed by Triplett et al.[9] and Niu et al.[11]. The deviation partly results from the larger size of circular microchannel and different junction configurations used in their study as shown in Figure 2-2.

Due to its relatively stable and preferable characteristics for mass transfer, only gas-liquid flow in the slug flow regime was investigated in the following study. In order to be more intuitive, the gas phase in slug flow is named bubble.

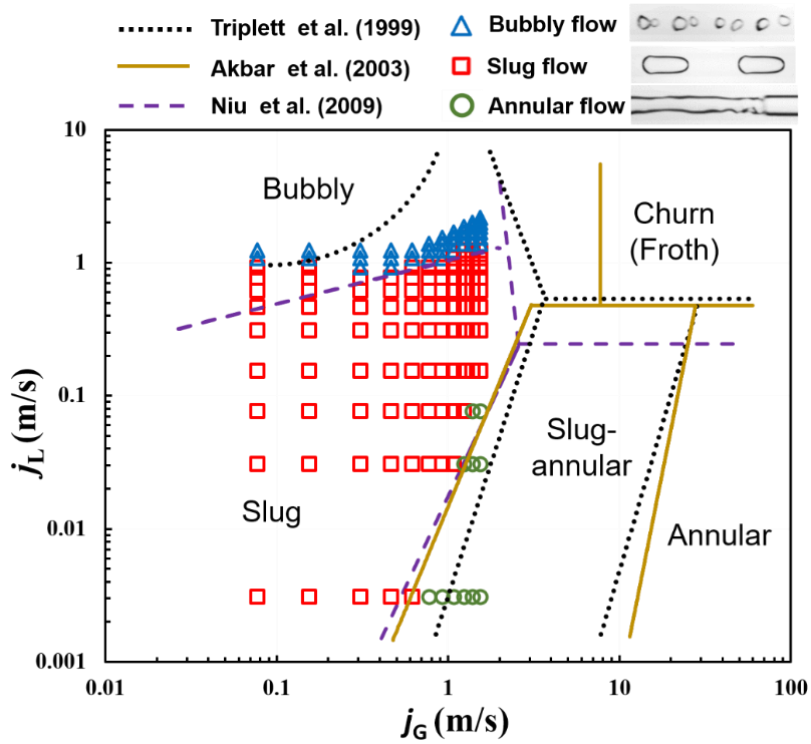

Figure 4-1 Flow pattern map of square microchannel. (superficial gas and liquid velocity are calculated by j_G and j_L).

4.1.2 Scaling law

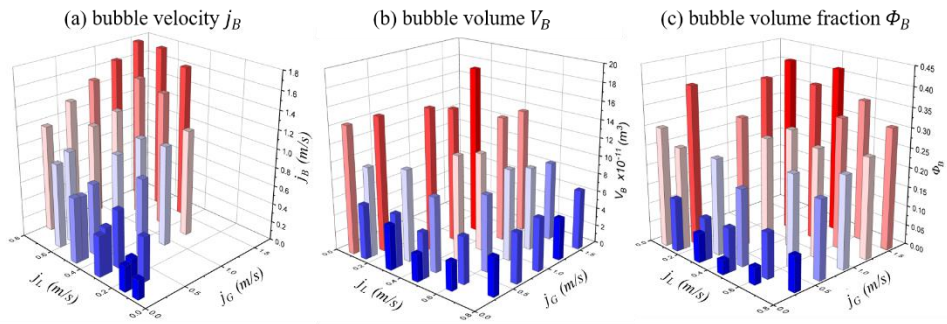

Figure 4-2 bar charts of parameters of rectangular microchannel against superficial gas and liquid velocities: (a) bubble velocity j_B; (b) bubble volume V_B; (c) bubble volume fraction Φ_B.

Figure 4-2 demonstrates the effect of superficial gas and liquid velocities on bubble velocity and volume. As shown in Figure 4-2 (a), the bubble velocity shows remarkably positive relationships with superficial gas and liquid velocities. As shown in Figure 4-2 (b), the bubble volume is larger at the higher superficial gas velocity and lower superficial liquid velocity. The reason is related to the time for bubble to grow and break up. Bubble volume fraction in Figure 4-2 (c) shows the same trend.

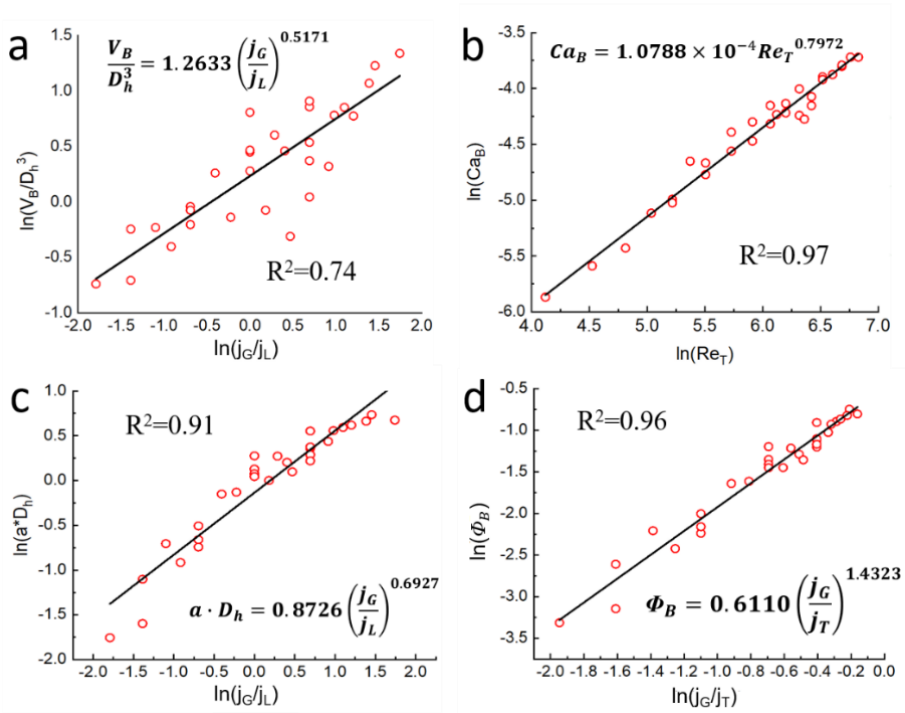

Figure 4-3 Correlations of hydrodynamics of the bubbles in rectangular microchannel.

$$\frac{V_B}{D_h^3} = 1.2633\left(\frac{j_G}{j_L}\right)^{0.5171} \tag{4-1}$$

$$Ca_B = 1.0788 \times 10^{-4} Re_T^{0.7972} \tag{4-2}$$

$$a \cdot D_h = 0.8726\left(\frac{j_G}{j_L}\right)^{0.6927} \tag{4-3}$$

$$\Phi_B = 0.6110\left(\frac{j_G}{j_T}\right)^{1.4323} \tag{4-4}$$

Figure 4-3 shows the scaling lows about the bubble properties and dimensionless numbers in rectangular microchannel, including bubble volume V_B, superficial gas and liquid velocity j_G and j_L, total superficial velocity j_T, Capillary number Ca_B, Reynolds number Re_T,

specific interfacial area a and bubble volume fraction Φ_B. The correlations were fitted as shown in Eq. (4-1,2,3,4). They all show a good fitting result. The coefficient of determination R^2 is higher than 0.7.

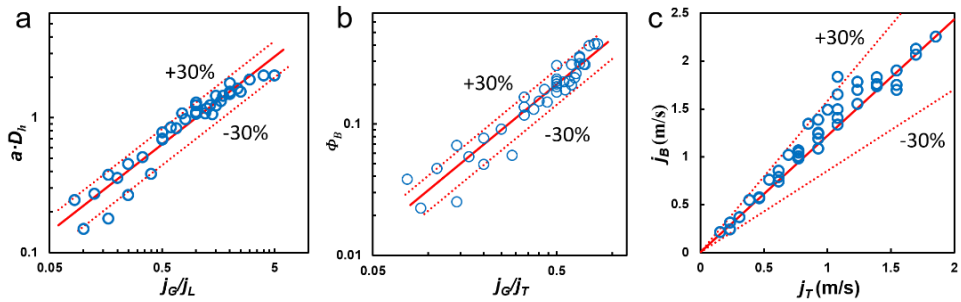

Figure 4-4 Correlations of square microchannel: (a) specific interfacial area; (b) bubble volume fraction; (c) bubble velocity.

$$a \cdot D_h = \left(\frac{j_G}{j_L}\right)^{0.6530} \tag{4-5}$$

$$\Phi_B = 0.4470 \left(\frac{j_G}{j_T}\right)^{1.1560} \tag{4-6}$$

$$j_B = 1.2175 \cdot j_T \tag{4-7}$$

In order to explore the influence of cross section on the scaling laws, scaling lows in square microchannel were fitted, by using bubble properties including the specific interfacial area a, bubble volume fraction Φ_B, superficial gas and liquid velocity j_G and j_L, bubble velocity j_B and total superficial velocity j_T. Figure 4-4 shows a good fitting result for all correlations. All the points are almost within $\pm 30\%$ error bound.

By comparing the scaling laws of square and rectangular microchannels, the coefficients in correlations of $a \cdot D_h$ and Φ_B are very close. Therefore, these correlations have a significant universality. All in all, these scaling laws can provide the guidance for the design of micro-reactors. They played an important role in the estimation of important parameters in micro-reactors, such as the ratio of the feed volume of reactant streams and residence time.

4.1.3 Mass transfer coefficient

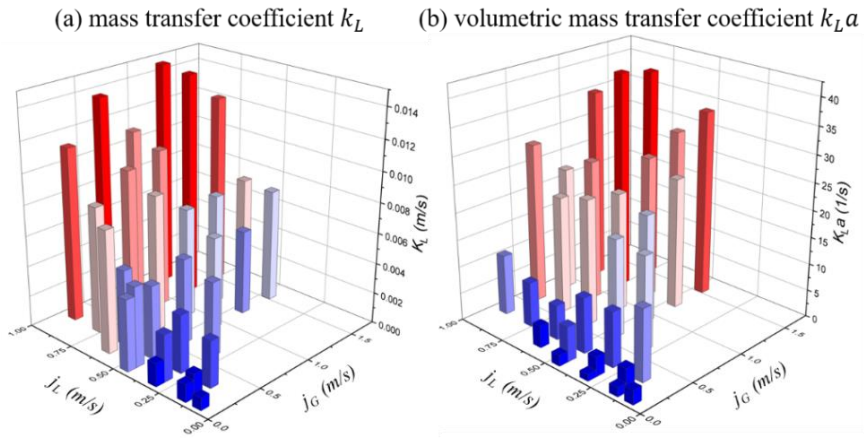

Figure 4-5 Effect of the superficial gas and liquid velocity on mass transfer in rectangular microchannel (a) mass transfer coefficient k_L; (b) volumetric mass transfer coefficient $k_L a$.

By calculating bubble volume and interface area, the mass transfer from gas phase to liquid phase in rectangular and square microchannels was estimated. Figure 4-5 shows the effect of superficial gas and liquid velocity on mass transfer coefficients in rectangular microchannel. Mass transfer coefficient k_L and volumetric mass transfer coefficient $k_L a$ both show the significant positive relationship with superficial gas and liquid velocity. It is because the higher superficial gas and liquid velocities, the stronger internal circulation and the renewal of liquid at the interface.

(a) Rectangular microchannel

	Geometry of cross section	Hydraulic diameter D_h	Cross section	Junction
Yue at el. 2006	1000 × 500 μm	667μm	rectangular	Y-shaped
Li at el.	400 × 600 μm	480μm	rectangular	T-shaped
Yue at el. 2009	400 × 400 μm	400μm	square	Y-shaped
Niu at el.	1000μm	1000μm	circular	T-shaped

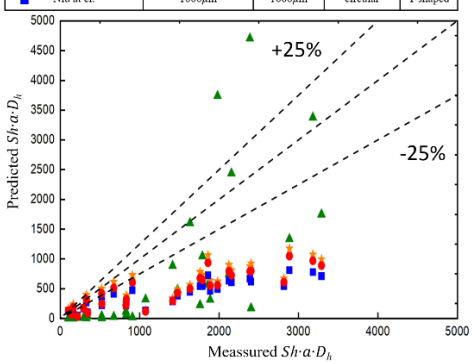

(b) Square microchannel

	Geometry of cross section	Hydraulic diameter D_h	Cross section	Junction
Yue et al.	1000 × 500 μm	667 μm	rectangular	Y-shaped
Yao et al.	600 × 300 μm	400 μm	rectangular	T-shaped
Bercic and Pintar	D_C: 1500, 2500, 3100 μm	1500,2500,3100 μm	circular	/
Van Baten et al.	D_C: 1500, 2000, 3000 μm	1500,2000,3000 μm	circular	/

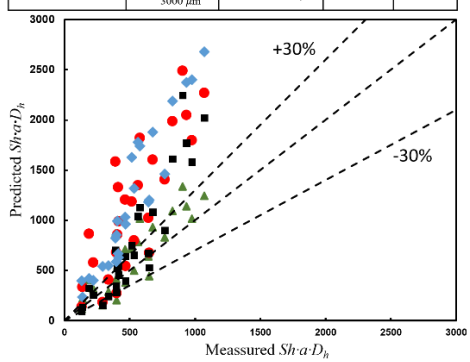

Figure 4-6 (a) Comparison between the experimental $Sh \cdot a \cdot D_h$ in rectangular microchannel and predictions of correlations in literatures [64-67]; (b) Comparison between the experimental $Sh \cdot a \cdot D_h$ in square microchannel and predictions from pure empirical correlations[65, 68, 69] and the theoretical model [70](Eq. (4-13)) in the literature.

Many correlations based on dimensionless numbers were developed to predict dimensionless number $Sh \cdot a \cdot D_h = k_L a D_h^2 / D_{dif}$. $Sh \cdot a \cdot D_h$ can consider simultaneously the important effect on mass transfer process, including mass transfer coefficients, diffusion rate, specific interfacial area of bubble and size of microchannel. Figure 4-6 shows the comparison between the present measured values and the predicted values from typical correlations of $Sh \cdot a \cdot D_h$ in literature of rectangular microchannel [64-67] and square microchannel [65, 68, 69]. Like this study, these correlations were all developed based on CO_2 absorption in water. However, the correlations all underestimated the mass transfer in the rectangular microchannel. In the square microchannel, the correlations overestimate the measured values in square microchannel except Yue et al. [65]. The correlation proposed by Yue et al. [65] can properly predict our measured data, because of similar hydraulic diameters of square microchannel. The differences in hydraulic diameter, type of junction and shape of the cross-section may be the reason of deviation. Therefore, it is necessary to develop new correlations that can accurately predict mass transfer coefficient in rectangular and square microchannels.

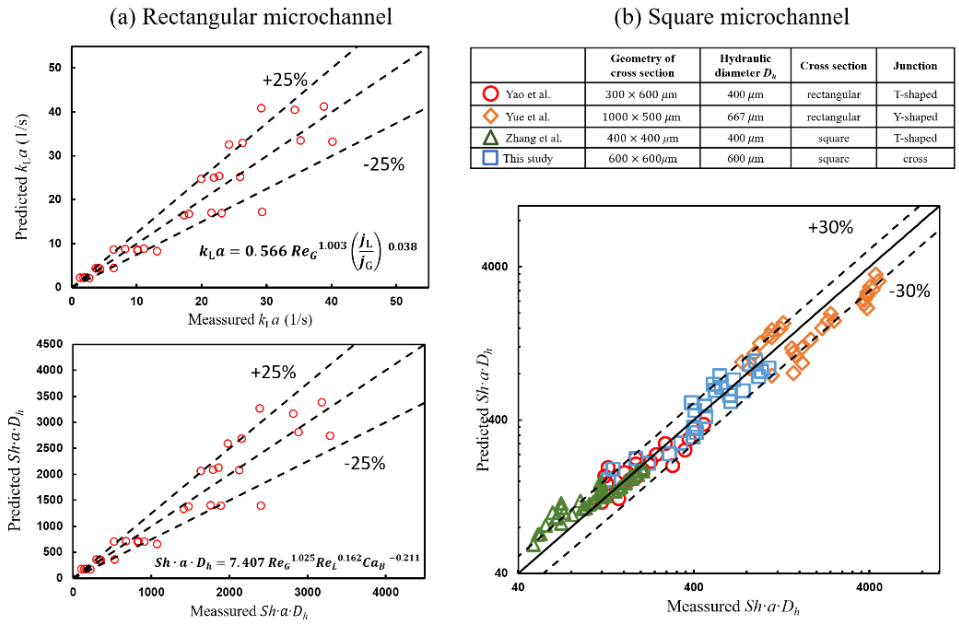

	Geometry of cross section	Hydraulic diameter D_h	Cross section	Junction
Yao et al.	300 × 600 μm	400 μm	rectangular	T-shaped
Yue et al.	1000 × 500 μm	667 μm	rectangular	Y-shaped
Zhang et al.	400 × 400 μm	400 μm	square	T-shaped
This study	600 × 600μm	600 μm	square	cross

Figure 4-7 (a) The comparison between measured values from rectangular microchannel and predictions of Eq. (4-8) and Eq. (4-9). (b) Comparison between the measured $Sh \cdot a \cdot D_h$ (based on the data from square microchannel and literature data[17, 21, 65]) and the predicted $Sh \cdot a \cdot D_h$ from the empirical correlation Eq. (4-10).

As for rectangular microchannel,

$$k_L a = 0.566\ {Re_G}^{1.003} \left(\frac{j_L}{j_G}\right)^{0.038} \tag{4-8}$$

$$Sh \cdot a \cdot D_h = 7.407\ {Re_G}^{1.025} {Re_L}^{0.162} {Ca_B}^{-0.211} \tag{4-9}$$

As for square microchannel,

$$Sh \cdot a \cdot D_h = 0.9566 \cdot {Re_G}^{0.5698} \cdot {Re_L}^{0.2296} \cdot {Sc_L}^{0.5} \tag{4-10}$$

By using the experiment data in rectangular microchannel, the correlations of $k_L a$ and $Sh \cdot a \cdot D_h$ were fitted based on dimensionless numbers as shown in Eq. (4-8) and Eq. (4-9).

Figure 4-7 (a) shows the comparison between measured values and predicted values of correlations Eq. (4-8) and Eq. (4-9). The correlations both have good predicted performance, and they can predict the mass transfer within ± 25% error band. It should be noted that the index of dimensionless numbers is close to 0 except Re_G, which means that the mass transfer process may be mainly related to gas flow conditions. This sparked our interest in continuing to explore mass transfer in square microchannel.

A correlation Eq. (4-10) based on dimensionless numbers was fitted to predict $Sh \cdot a \cdot D_h$ in square microchannel. Figure 4-7 (b) shows that blue square points locate within ± 30% error bound, confirming that the correlation Eq. (4-10) can precisely predict the measured values in square microchannel. Besides, the correlation Eq. (4-10) also shows excellent prediction performance to predict the measured $Sh \cdot a \cdot D_h$ in literature[17, 21, 65], even though channel geometry, shape of cross-section and junction are different. The error is also within a ± 30% bound.

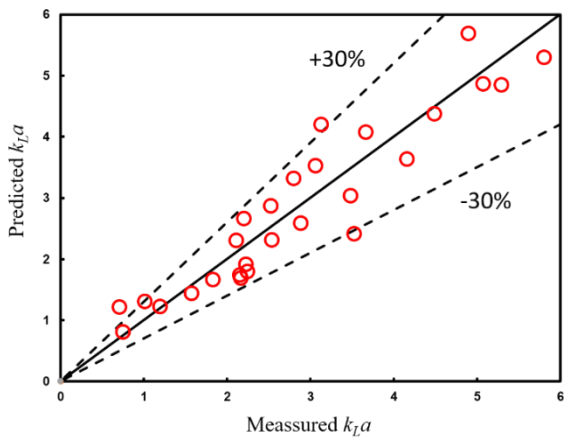

Figure 4-8 Comparison between the measured $k_L a$ from square microchannel and the predicted $k_L a$ from semi-theoretical model Eq. (4-14).

Although empirical correlation Eq. (4-10) shows a good prediction performance, there are still restrictions due to the limited database. In contrast, theoretical models are more convincing. A fundamental model based on two contributions to the mass transfer process was developed by Van Baten et al.[70]. The contributions consist of mass transfer between the film and the bubble body and mass transfer between two bubble caps and the liquid plug. Penetration theory[71] was used to derive the model:

$$(k_L a)_{film} = 2\sqrt{\frac{D_{dif} j_G}{\pi L_f}} \cdot \frac{4L_f}{L_C D_h} \tag{4-11}$$

$$(k_L a)_{caps} = 2\frac{\sqrt{2}}{\pi}\sqrt{\frac{D_{dif} j_G}{D_h}} \cdot \frac{4}{L_C} \tag{4-12}$$

Here, D is the diffusivity, L_f is the length of the film, D_h is the hydraulic diameter. After validation of CFD simulation, the total volumetric mass transfer coefficient $k_L a$ is calculated:

$$k_L a = (k_L a)_{film} + (k_L a)_{caps} \tag{4-13}$$

However, Figure 4-6 (b) shows that the predicted values by Eq. (4-13) deviated from the measured values. It is because deformed bubbles in the square channel caused the non-uniform film and asymmetrical caps. It is not accurate to directly apply the sum of the contributions for deformed bubbles. According to bubble visualizations in Figure 2-6, the ratio of the length of liquid phase and gas phase, i.e., $\frac{L_L}{L_G}$ can characterize the degree of bubble deformation. Therefore, a new semi-theoretical model was proposed by including $\frac{L_L}{L_G}$:

$$k_L a = 0.3469 \cdot (k_L a)_{caps} + 0.4806 \cdot (k_L a)_{film} \cdot \left(\frac{L_L}{L_G}\right)^{0.5012} \tag{4-14}$$

As shown in Figure 4-8, the new semi-theoretical model Eq. (4-14) can predict the measured $k_L a$ accurately within ± 30% error bound.

4.2 Porous media with microchannel network

4.2.1 Fingering pattern and morphology

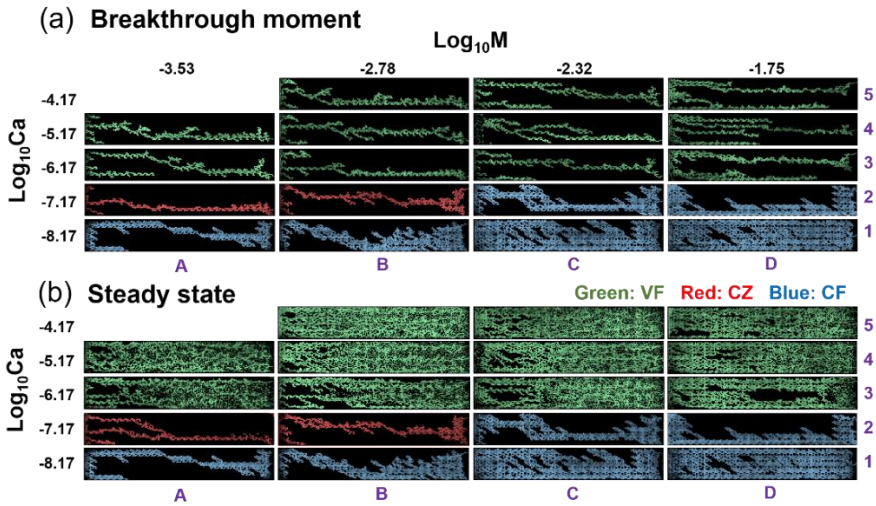

Figure 4-9 Visualization of finger morphologies at the breakthrough moment and at the steady state for three different flow regions as a function of the viscosity ratio $Log_{10}M$ and the capillary number $Log_{10}Ca$: (a) morphologies at the breakthrough moment when the finger cap reaches the outlet; (b) morphologies at the steady state when invasion area no longer increases.

Figure 4-9 shows the fingering morphologies at the breakthrough moment and steady state in different flow regions. For convenience, the symbols with letters and numbers (A1, A2…D4, D5) were used to represent the different cases. The cases include the regions of viscous fingering (VF), capillary fingering (CF) and crossover zone (CZ). In VF region, the viscous force mainly controls the fingering displacement process, which allows gas to invade forward rather than lateral. A narrow and straight flow path is generated in the green patterns of Figure 4-9 (a). After breakthrough, the gas will continue to invade liquid. At steady state, almost all the liquid phase is displaced as shown in Figure 4-9 (b). Capillary fingering is located in the region with lower $Log_{10}Ca$ and higher $Log_{10}M$ as shown in Figure 4-9 (a). Due to the lower velocity of the invading phase and the lower viscosity of the defending phase, the viscous force can be neglected and the capillary force mainly controls the displacement process. The gas will mainly spread lateral channels, and thus a wide finger forms. After breakthrough, displacement stops as shown in the blue patterns of Figure 4-9 (b). The red patterns of Figure 4-9 demonstrate that the finger in crossover zone will expand a little bit area after breakthrough. It is because the capillary force and viscous force jointly control fingering displacement process.

4.2.2 Comparative quantification

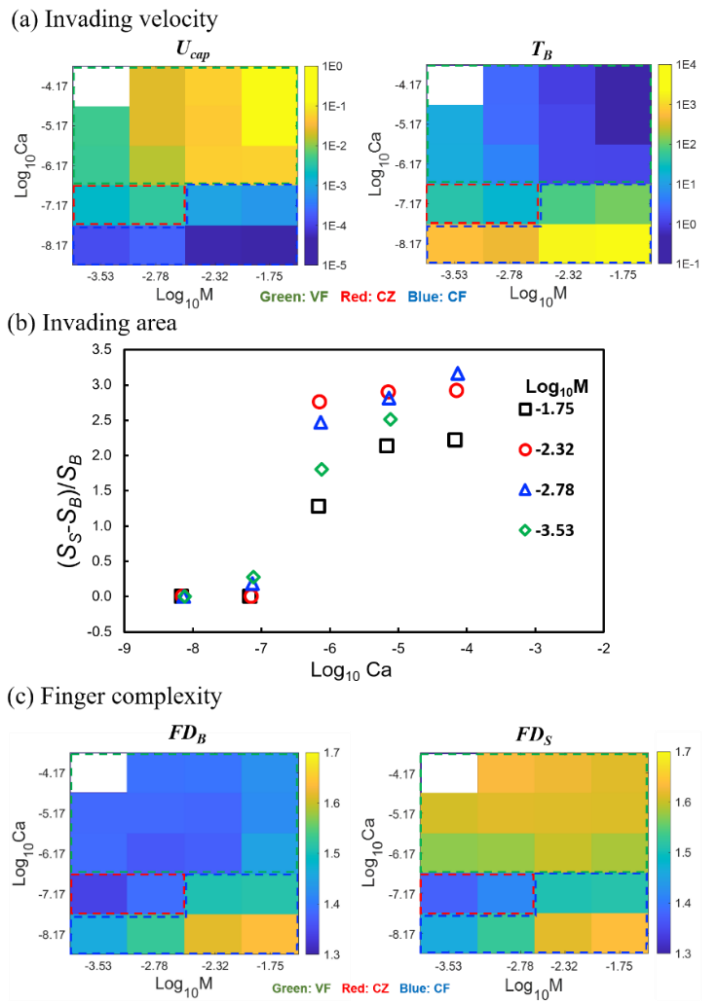

Figure 4-10 (a) Map of the finger cap velocity U_{cap} and breakthrough time T_B; (b) saturation gain ratio$(S_S - S_B)/S_B$; (c) Map of fractal dimension FD_B at the breakthrough moment and FD_S at the steady state. (VF region: green dotted rectangle; CZ region: red dotted rectangle; CF region: blue dotted rectangle).

The detailed quantitative analysis of the fingering displacement and patterns was conducted.

Invasion velocity:

Figure 4-10 (a) shows velocity map of the finger cap U_{cap} and breakthrough time T_B with the function of $Log_{10}Ca$ and $Log_{10}M$. U_{cap} was obtained by fitting the slope of the curve of

fingering cap position versus time. T_B is the elapsed time for the finger cap to invade from the inlet to the outlet. U_{cap} is fastest and T_B is shortest in VF region as shown in Figure 4-10 (a). Invasion velocity has a positive relationship with $Log_{10}Ca$ and $Log_{10}M$ in VF region because of higher gas flow rate and weaker resistance. The minimum time to breakthrough is only 0.48 s at the highest $Log_{10}M$ and $Log_{10}Ca$. T_B in the CF region is about 4 orders of magnitude higher than the shortest time, which demonstrates that the displacement patterns have a significant impact on the invading velocity.

Invasion area:

The saturation was also measured to characterize the invasion area. By measuring fingering area A_{BT} and A_{SS}, the saturation at the breakthrough moment and the steady state were calculated based on Eq.(4-15) and Eq.(4-16).

$$S_B = \frac{A_{BT}}{LW\varphi} \tag{4-15}$$

$$S_S = \frac{A_{SS}}{LW\varphi} \tag{4-16}$$

Figure 4-10 (b) presents the saturation gain ratio $(S_S - S_B)/S_B$, which is the normalized increment of saturation from the breakthrough moment to steady state. The saturation gain ratio is equal to zero in CF region because gas stops expanding new area after breakthrough. The gas with a low flow rate can only flow along the previously formed invading paths after breakthrough. Saturation gain ratio increases to ranges from 1.0 to 3.0 in the VF region, because gas continues to invade new area after breakthrough. The invaded area increases significantly after breakthrough in the VF region. It is validated by previous experimental observations of fingering morphologies in Figure 4-9.

Finger complexity:

Finger complexity can be quantified by fractal dimension FD, which was calculated by box-counting method [72]. By fitting the curve of boxes number N occupied by the pattern as a function of the resolution scale Δ (size of box), the FD at the breakthrough moment and the steady state can be calculated by Eq. (4-17).

$$FD = \lim_{\Delta \to \infty} \frac{log(N)}{log(\Delta)} \tag{4-17}$$

As shown in Figure 4-10 (c), FD grows from about 1.4 to 1.6 in the VF region after breakthrough, while the fingering complexity keeps same in CF region after breakthrough. This is consistent with the observation of invasion area. More invasion area represents the formation of more finger branches and correspondingly FD grows.

The comparative quantitative research before and after breakthrough provides potential guidance on how to achieve high displacement efficiency in a relatively short time and whether it is cost-effective to continue gas injection after breakthroughs in industrial applications.

4.2.3 Dynamical fingering evolution

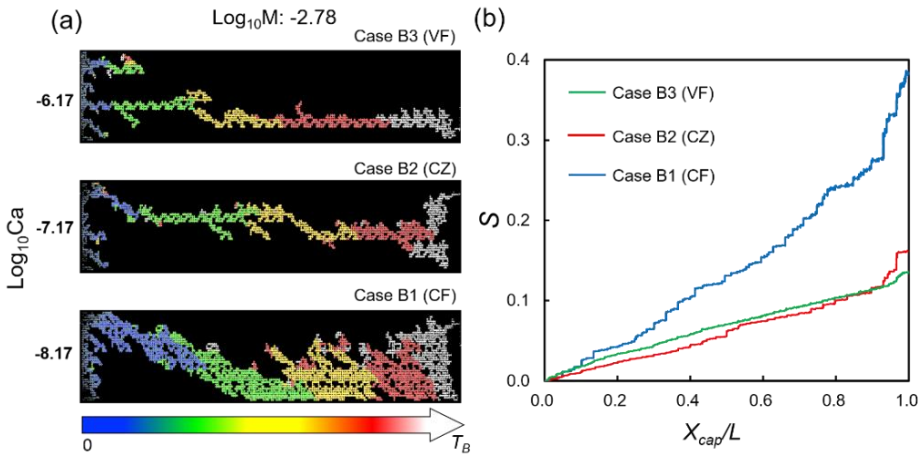

Figure 4-11 Gas invading process and evolution of fingering patterns before breakthrough: (a) finger evolution of invasion process in VF (Case B3), CZ (Case B2) and CF (Case B1) regions until breakthrough, respectively; (b) corresponding saturation curve as a function of the normalized location of finger cap X_{cap}/L, where L is the length of porous media domain.

Figure 4-11 (a) shows the gas displacement process before breakthrough. To intuitively show the displaced location in each period, images were painted in different colors according to different periods from 0 to T_B. In the earlier period (painted in blue), the displacement is compact. As the displacement progresses, the compact displacement is broken by one or two preferential flow paths (painted in green). The interface gradually becomes unstable. A sudden rise in fingering branches occurs in the final period of invasion (painted in white). So, the sudden increase at the end of the saturation curves in Figure 4-11 (b) can be observed. It is more prominent in the CZ and CF regions. Because The capillary dispersion effect allows the cap to invade the branches. It is also interesting to observe the minor newly displaced area (painted in red and white) appears near the inlet in the VF region close to breakthrough, which strongly motivates us to explore the fingering evolution from breakthrough to steady state.

As shown in Figure 4-12 (a), dramatic changes of fingering patterns are observed in the VF regime after breakthrough. Figure 4-12 (a) illustrates the fingering evolution in VF region from breakthrough moment T_B to steady state T_S. Most of the displaced area is located near the outlet except for case D3, leaving the uninvaded area near the inlet. As the decrease of liquid viscosity (increase of $Log_{10}M$), the saturation reaches S_S in earlier times. As illustrated by the curves of S in Figure 4-12 (b), the slope of saturation curves shows a positive relationship with $Log_{10}M$. It is because the lower liquid viscosity, the weaker resistance. The curves are approximately linear before T_B. Fluctuation begin to occur after T_B. After the turning point indicated by the dotted circles, the curves flatten and steady state T_S reaches.

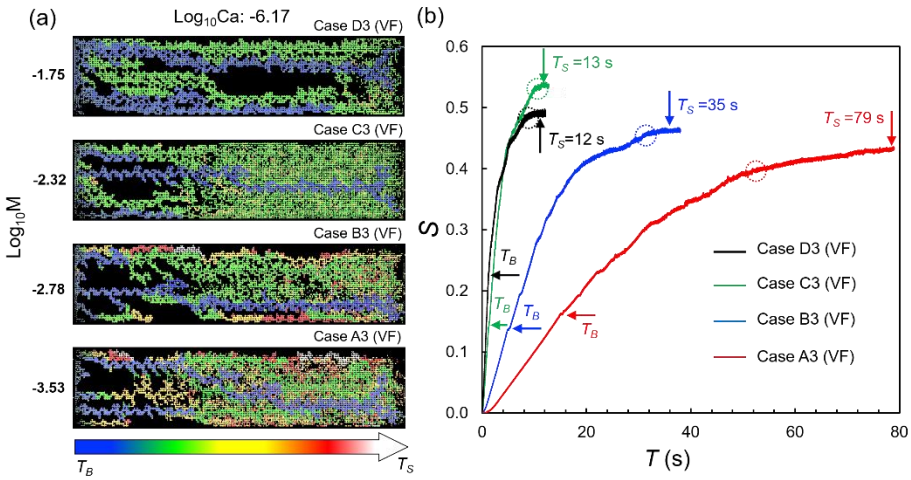

Figure 4-12 Invading process and finger evolution from breakthrough to steady state in VF region. (a) evolution of invasion process after breakthrough (painted in different colors according to different periods); (b) saturation curve as a function of the elapsed time T.

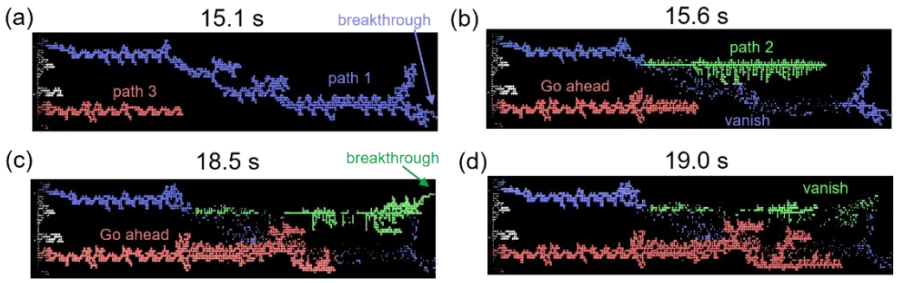

Figure 4-13 Time evolution of fingering after breakthrough in VF region at the case A3, where different paths were painted in different colors.

In order to dig into the underlying mechanism, time evolution of fingering after breakthrough in VF region is analyzed. Taking case A3 as an example, a previously unobserved finger vanishing and re-forming cycle was found. Figure 4-13 (a) illustrates that path 1 breakthrough preferentially compared with path 3. After a short time of about 0.5 s, the front part of path 1 disappears, leaving the disconnected ganglia (Figure 4-13 (b)). Such fingering instability is originally caused by the sudden decrease of the entry pressure P_C at breakthrough moment, which can be estimated by:

$$P_C = \frac{2\sigma \cos\theta_R}{r} \tag{4-18}$$

Entry pressure is calculated as about 2000 Pa by using receding contact angle θ_R of 30° and throat size r of 63 μm. After breakthrough, high entry pressure is released. Air only needs to

overcome the relatedly lower flow resistance. So, the front part of path 1 escapes fast. A similar phenomenon also can be found in previous research [73]. The finger vanishing and disconnected ganglia will quickly restore the pressure, which facilitates the generation of new path 2. After about 3 s, path 2 breaks through and becomes disconnected as shown in Figure 4-13 (c). Similar to path 1, the front part of path 2 disappears after about 0.5 s, leaving scattered dots (Figure 4-13 (d)). All in all, each path will repeat a process, including new finger forming, cap invading, breakthrough and finger vanishing. Until saturation reaches the maximum, a steady state reaches.

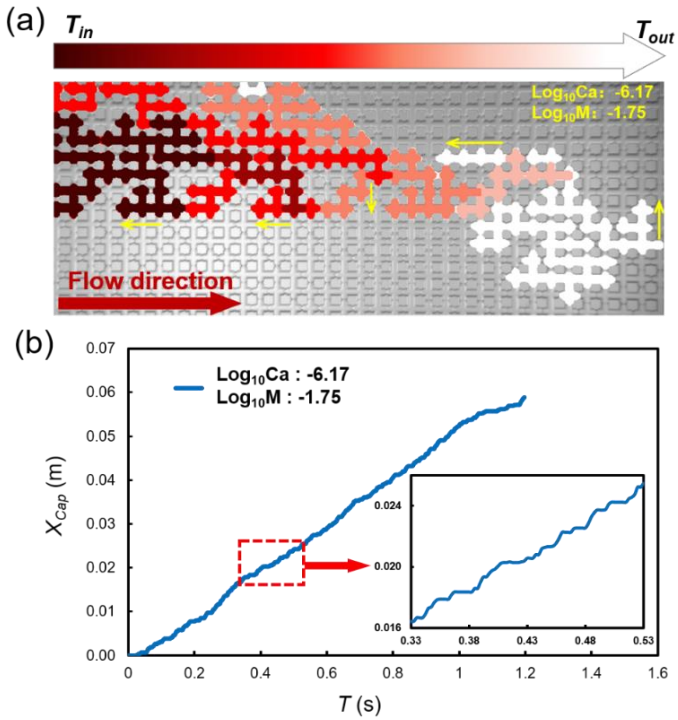

Figure 4-14 (a) local dynamical invasion behavior captured by high-speed camera with macro lens (painted in different colors according to different periods); (b) curve of fingering cap position over time.

To explore the local dynamical invasion behavior, the reduced visualization window was monitored as shown in Figure 4-14 (a). The cap of fingering moves forward with time T. As shown in the yellow arrows of Figure 4-14 (a), the cap stop moves forward and its gas branches expand in other directions, especially in backward direction. It is because the driving pressure has not yet accumulated large enough to overcome the forward entry pressure. After the accumulated pressure is enough, the cap will continue to invade forward. This process can be verified by the curve of finger cap position over time in Figure 4-14 (b). As shown in Figure 4-14 (b), the gas cap moves in a stepwise way.

CHAPTER 5

Conclusions and Outlook

5.1 Conclusions

This thesis aims to investigate gas-liquid two-phase flow in microscale, including slug flow in the microchannel and gas-liquid displacement in porous media with microchannel network. In the interaction process of gas-liquid two-phase flow, mass transfer or interfacial instability is accompanied. In order to reveal the underlying mechanism, the microfluidics platforms with a high-speed imaging system were built to investigate the mass transfer of slug flow in microchannels and interfacial instability in porous media:

Rectangular and square microchannels:

- Flow patterns and behavior were captured by a high-speed imaging system. Depending on different flow rates, gas-liquid flow patterns in the microchannels include slug flow, bubbly flow, and annular flow. Flow pattern map was proposed and compared with the maps in literatures.
- In order to measure the bubble volume in rectangular and square microchannels, the bubble reconstruction methods were developed based on 2D projection and 3D slicing, correspondingly. The important parameters in micro-reactors were quantified. Scaling laws were derived to predict these parameters, which can provide the guidance of microreactor design.
- Based on the rate of change in CO_2 bubble volume, the mass transfer coefficients in rectangular and square microchannels were calculated. It is found that mass transfer coefficients are positively dependent on gas and liquid flow rates.
- Finally, the new empirical correlations involving dimensionless numbers were developed to predict the mass transfer coefficients. Further, to have a better universality, a semi-theoretical model, considering the length ratio of liquid and gas phases L_L/L_G in square microchannel, was developed. Empirical correlations and

semi-theoretical model both show a good predictive capability to predict the measured values accurately within ± 30% error bound.

Porous media with microchannel network:

- Gas-liquid displacement processes before and after breakthrough in a porous media chip were captured by experimental flow imaging. With a wide range of capillary numbers Ca and viscosity ratios M, the flow region can cover viscous fingering (VF), capillary fingering (CF) and crossover zone (CZ). Visualization of the fingering morphologies illustrates that capillary fingering stops displacement after breakthrough, whereas viscous fingering can continue to expand until almost all the liquid phase is displaced.
- Imperative quantitative studies in terms of invasion velocity, invading area and fingering complexity were conducted based on digital image processing. It is found that displaced areas expand significantly after breakthrough in VF region. It indicates that evolution of fingering patterns after breakthrough is well worth exploring.
- Fingering dynamical behaviors before and after breakthrough were analyzed. Firstly, compact displacement area is generated near inlet, then it is broken by one or two preferential flow paths. When the fingering approaches the outlet, a sudden rise in fingering branches occurs. After Breakthrough, most displaced area is located near the outlet. The saturation curves keep linear before breakthrough, and begin to fluctuate after breakthrough. Then the curves flatten and a steady state reaches.
- By analyzing time evolution of fingering after breakthrough, a previously unobserved circle was discovered, involving new finger generation, cap invading, breakthrough and finger vanishing. This process will repeat until steady state. Analysis of local dynamical invasion behavior exposes a stepwise way of fingering cap movement. The fingering cap will temporarily stop invading forward and its branches will expand in other directions especially backward when accumulated gas pressure is not sufficient to overcome the forward entry pressure.
- This research is of significance in subsurface applications in terms of evaluating extraction effectiveness, economic benefits and storage safety.

5.2 Outlook

Microchannel:

- Breakup hydrodynamic at the junction is of great significance in two-phase flow in microchannels. Although extensive work has been devoted to revealing the underlying mechanism, a reliable theoretical model has not been established.
- Fluid properties also have an important impact on mass transfer in microchannels, such as viscosity, surface tension and wettability. The design of microreactors also needs to consider fluid properties, so it will be investigated in the next research.
- CFD simulation is a powerful tool to investigate two-phase flow in microchannel. Three-dimensional bubbles shape can be simulation. Numerical result can further verify the volume calculation methods in this thesis.

Porous media with microchannel network:

- 2D porous media chip was used in this thesis. However, in reality, porous media structure is three-dimensional. Therefore, the investigation of immiscible displacement in a realistic 3D configuration is more meaningful.
- Capillary pressure, determined by microchannel size, surface tension of fluid and contact angle of fluid on channel wall, is a driving force for wetting fluids through microchannels, while is a resistance for no-wetting fluids. Although simulation has been used to explore the influence of wettability of fluid on the interfacial instability, it still needs experimental validation.
- Lattice Boltzmann simulation is an appropriate method to study flows at the microscale. Numerical simulation can measure some important parameters that cannot or is difficult to be obtained from the experiment method. In addition, simulations can be cross-validated with experiments.

References

[1] A. Manz, N. Graber, H.á. Widmer, Miniaturized total chemical analysis systems: a novel concept for chemical sensing, Sensors actuators B: Chemical, 1(1-6) (1990) 244-248.

[2] J. McGinty, V. Svoboda, P. Macfhionnghaile, H. Wheatcroft, C.J. Price, J. Sefcik, Continuous crystallisation of organic salt polymorphs, Frontiers in Chemical Engineering, 4 (2022).

[3] H.M. Hegab, A. ElMekawy, T. Stakenborg, Review of microfluidic microbioreactor technology for high-throughput submerged microbiological cultivation, Biomicrofluidics, 7(2) (2013) 021502.

[4] B.S. Ferguson, S.F. Buchsbaum, T.-T. Wu, K. Hsieh, Y. Xiao, R. Sun, H.T. Soh, Genetic analysis of H1N1 influenza virus from throat swab samples in a microfluidic system for point-of-care diagnostics, Journal of the American Chemical Society, 133(23) (2011) 9129-9135.

[5] C.D. Edington, W.L.K. Chen, E. Geishecker, T. Kassis, L.R. Soenksen, B.M. Bhushan, D. Freake, J. Kirschner, C. Maass, N. Tsamandouras, Interconnected microphysiological systems for quantitative biology and pharmacology studies, Scientific reports, 8(1) (2018) 1-18.

[6] J. Yue, G. Chen, Q. Yuan, L. Luo, Y. Gonthier, Hydrodynamics and mass transfer characteristics in gas-liquid flow through a rectangular microchannel, Chemical Engineering Science, 62(7) (2007) 2096-2108.

[7] Z. Wu, B. Sundén, Liquid-liquid two-phase flow patterns in ultra-shallow straight and serpentine microchannels, Heat and Mass Transfer, 55(4) (2019) 1095-1108.

[8] M. Sattari-Najafabadi, M. Nasr Esfahany, Z. Wu, B. Sunden, Mass transfer between phases in microchannels: A review, Chemical Engineering and Processing - Process Intensification, 127 (2018) 213-237.

[9] K.A. Triplett, S. Ghiaasiaan, S. Abdel-Khalik, D. Sadowski, Gas–liquid two-phase flow in microchannels Part I: two-phase flow patterns, International Journal of Multiphase Flow, 25(3) (1999) 377-394.

[10] M. Akbar, D. Plummer, S.M. Ghiaasiaan, On gas-liquid two-phase flow regimes in microchannels, International Journal of Multiphase Flow, 29(5) (2003) 855-865.

[11] H. Niu, L. Pan, H. Su, S. Wang, Flow pattern, pressure drop, and mass transfer in a gas-liquid concurrent two-phase flow microchannel reactor, Industrial and Engineering Chemistry Research, 48(3) (2009) 1621-1628.

[12] O. Baker, Design of pipelines for the simultaneous flow of oil and gas, in: Fall meeting of the petroleum branch of AIME, OnePetro, 1953.

[13] C. Yao, Y. Zhao, H. Ma, Y. Liu, Q. Zhao, G. Chen, Two-phase flow and mass transfer in microchannels: A review from local mechanism to global models, Chemical Engineering Science, 229 (2021) 116017.

[14] R. Lindken, M. Rossi, S. Große, J. Westerweel, Micro-particle image velocimetry (μPIV): recent developments, applications, and guidelines, Lab on a Chip, 9(17) (2009) 2551-2567.

[15] Q. Li, P. Angeli, Experimental and numerical hydrodynamic studies of ionic liquid-aqueous plug flow in small channels, Chemical Engineering Journal, 328 (2017) 717-736.

[16] W.G. Whitman, The two-film theory of gas absorption, Chem. Metall. Eng., 29 (1923) 146-148.

[17] Y. Zhang, C. Zhu, C. Chu, T. Fu, Y. Ma, Mass transfer and capture of carbon dioxide using amino acids sodium aqueous solution in microchannel, Chemical Engineering Processing-Process Intensification, 173 (2022) 108831.

[18] Y. Chen, C. Zhu, T. Fu, Y. Ma, Mass transfer enhancement of CO_2 absorption into [Bmim][BF4] aqueous solution in microchannels by heart-shaped grooves, Chemical Engineering Processing-Process Intensification, 167 (2021) 108536.

[19] C. Zhu, C. Li, X. Gao, Y. Ma, D. Liu, Taylor flow and mass transfer of CO_2 chemical absorption into MEA aqueous solutions in a T-junction microchannel, International Journal of Heat and Mass Transfer, 73 (2014) 492-499.

[20] C. Yao, Y. Liu, S. Zhao, Z. Dong, G. Chen, Bubble/droplet formation and mass transfer during gas–liquid–liquid segmented flow with soluble gas in a microchannel, AIChE Journal, 63(5) (2017) 1727-1739.

[21] C. Yao, Z. Dong, Y. Zhao, G. Chen, An online method to measure mass transfer of slug flow in a microchannel, Chemical Engineering Science, 112 (2014) 15-24.

[22] X. Ye, T. Hao, Y. Chen, X. Ma, R. Jiang, Liquid film transport around Taylor bubble in a microchannel with gas cavities, Chemical Engineering Processing-Process Intensification, 148 (2020) 107828.

[23] L. Bai, S. Zhao, Y. Fu, Y. Cheng, Experimental study of mass transfer in water/ionic liquid microdroplet systems using micro-LIF technique, Chemical Engineering Journal, 298 (2016) 281-290.

[24] R.S. Abiev, C. Butler, E. Cid, B. Lalanne, A.-M. Billet, Mass transfer characteristics and concentration field evolution for gas-liquid Taylor flow in milli channels, Chemical Engineering Science, 207 (2019) 1331-1340.

[25] G.M. Homsy, Viscous fingering in porous media, Annual review of fluid mechanics, 19(1) (1987) 271-311.

[26] S. Hill, Channeling in packed columns, Chemical Engineering Science, 1(6) (1952) 247-253.

[27] P.G. Saffman, G.I. Taylor, The penetration of a fluid into a porous medium or Hele-Shaw cell containing a more viscous liquid, Proceedings of the Royal Society of London. Series A. Mathematical and Physical Sciences, 245(1242) (1958) 312-329.

[28] B. Zhao, C.W. MacMinn, R. Juanes, Wettability control on multiphase flow in patterned microfluidics, Proceedings of the National Academy of Sciences of the United States of America, 113(37) (2016) 10251-10256.

[29] T.T. Al-Housseiny, P.A. Tsai, H.A. Stone, Control of interfacial instabilities using flow geometry, Nature Physics, 8(10) (2012) 747-750.

[30] D. Pihler-Puzović, R. Périllat, M. Russell, A. Juel, M. Heil, Modelling the suppression of viscous fingering in elastic-walled Hele-Shaw cells, Journal of Fluid Mechanics, 731 (2013) 162-183.

[31] S.A. Aryana, A.R. Kovscek, Experiments and analysis of drainage displacement processes relevant to carbon dioxide injection, Physical Review E, 86(6) (2012) 066310.

[32] F. Furtado, F. Pereira, Crossover from nonlinearity controlled to heterogeneity controlled mixing in two-phase porous media flows, Computational Geosciences, 7(2) (2003) 115-135.

[33] D. Silin, T. Patzek, On Barenblatt's model of spontaneous countercurrent imbibition, Transport in porous media, 54(3) (2004) 297-322.

[34] J. Sun, Z. Li, F. Furtado, S.A. Aryana, A microfluidic study of transient flow states in permeable media using fluorescent particle image velocimetry, Capillarity, 4(4) (2021).

[35] T. Lan, R. Hu, Z. Yang, D.S. Wu, Y.F. Chen, Transitions of fluid invasion patterns in porous media, Geophysical Research Letters, 47(20) (2020).

[36] S.C. Cao, S. Dai, J. Jung, Supercritical CO_2 and brine displacement in geological carbon sequestration: Micromodel and pore network simulation studies, International Journal of Greenhouse Gas Control, 44 (2016) 104-114.

[37] R. Lenormand, E. Touboul, C. Zarcone, Numerical models and experiments on immiscible displacements in porous media, Journal of fluid mechanics, 189 (1988) 165-187.

[38] C. Zhang, M. Oostrom, T.W. Wietsma, J.W. Grate, M.G. Warner, Influence of viscous and capillary forces on immiscible fluid displacement: Pore-scale experimental study in a water-wet micromodel demonstrating viscous and capillary fingering, Energy Fuels, 25(8) (2011) 3493-3505.

[39] F. Guo, S.A. Aryana, An experimental investigation of flow regimes in imbibition and drainage using a microfluidic platform, Energies, 12(7) (2019) 1390.

[40] Y.F. Chen, S. Fang, D.S. Wu, R. Hu, Visualizing and quantifying the crossover from capillary fingering to viscous fingering in a rough fracture, Water Resources Research, 53(9) (2017) 7756-7772.

[41] I. Salmo, K. Sorbie, A. Skauge, M. Alzaabi, Immiscible Viscous Fingering: Modelling Unstable Water–Oil Displacement Experiments in Porous Media, Transport in Porous Media, (2022) 1-32.

[42] L. Mejia, M. Mejia, C. Xie, Y. Du, A. Sultan, K.K. Mohanty, M. Balhoff, Viscous Fingering of Irreducible Water During Favorable Viscosity Two-Phase Displacements, Advances in Water Resources, 153 (2021) 103943.

[43] H. Li, Pore-scale study on interfacial force-induced residue mobilization under immiscible ternary fluids flow, International Journal of Multiphase Flow, 147 (2022) 103913.

[44] M. Ruith, E. Meiburg, Miscible rectilinear displacements with gravity override. Part 1. Homogeneous porous medium, Journal of Fluid Mechanics, 420 (2000) 225-257.

[45] Y. Hu, A. Patmonoaji, C. Zhang, T. Suekane, Experimental study on the displacement patterns and the phase diagram of immiscible fluid displacement in three-dimensional porous media, Advances in Water Resources, 140 (2020) 103584.

[46] S. Yang, G. Kong, Z. Wu, Experimental Study of Gas-Liquid Displacement in a Porous Media Microchip by Digital Image Analysis Method, in: ASME International Mechanical Engineering Congress and Exposition, American Society of Mechanical Engineers, 2021, pp. V010T010A041.

[47] A. Scanziani, Q. Lin, A. Alhosani, M.J. Blunt, B. Bijeljic, Dynamics of fluid displacement in mixed-wet porous media, Proceedings of the Royal Society A: Mathematical, Physical and Engineering Sciences, 476(2240) (2020) 20200040.

[48] B. Levaché, D. Bartolo, Revisiting the Saffman-Taylor experiment: imbibition patterns and liquid-entrainment transitions, Physical review letters, 113(4) (2014) 044501.

[49] H.S. Rabbani, B. Zhao, R. Juanes, N. Shokri, Pore geometry control of apparent wetting in porous media, Scientific reports, 8(1) (2018) 1-8.

[50] F. Guo, S.A. Aryana, Y. Wang, J.F. McLaughlin, K. Coddington, Enhancement of storage capacity of CO_2 in megaporous saline aquifers using nanoparticle-stabilized CO_2 foam, International Journal of Greenhouse Gas Control, 87 (2019) 134-141.

[51] Y. Takeuchi, J. Takeuchi, M. Fujihara, Numerical investigation of inertial, viscous, and capillary effects on the drainage process in porous media, Computers Fluids, 237 (2022) 105324.

[52] Z. Wang, J.-M. Pereira, E. Sauret, S.A. Aryana, Z. Shi, Y. Gan, A pore-resolved interface tracking algorithm for simulating multiphase flow in arbitrarily structured porous media, Advances in Water Resources, 162 (2022) 104152.

[53] B.K. Primkulov, A.A. Pahlavan, X. Fu, B. Zhao, C.W. MacMinn, R. Juanes, Signatures of fluid–fluid displacement in porous media: wettability, patterns and pressures, Journal of Fluid Mechanics, 875 (2019).

[54] S.M. Hassanizadeh, W.G. Gray, Toward an improved description of the physics of two-phase flow, Advances in Water Resources, 16(1) (1993) 53-67.

[55] G. Barenblatt, T. Patzek, D. Silin, The mathematical model of non-equilibrium effects in water-oil displacement, in: Spe/doe improved oil recovery symposium, OnePetro, 2002.

[56] S.A. Aryana, A.R. Kovscek, Nonequilibrium effects and multiphase flow in porous media, Transport in porous media, 97(3) (2013) 373-394.

[57] Y. Wang, S.A. Aryana, F. Furtado, V. Ginting, Analysis of nonequilibrium effects and flow instability in immiscible two-phase flow in porous media, Advances in Water Resources, 122 (2018) 291-303.

[58] Y. Wang, S.A. Aryana, M.B. Allen, An extension of Darcy's law incorporating dynamic length scales, Advances in Water Resources, 129 (2019) 70-79.

[59] M. Musterd, V. Van Steijn, C.R. Kleijn, M.T. Kreutzer, Calculating the volume of elongated bubbles and droplets in microchannels from a top view image, RSC Advances, 5(21) (2015) 16042-16049.

[60] G. Kong, H. Mirsandi, K.A. Buist, E. Peters, M.W. Baltussen, J. Kuipers, Oscillation dynamics of a bubble rising in viscous liquid, Experiments in Fluids, 60(8) (2019) 1-13.

[61] R. Azadi, J. Wong, D.S. Nobes, Experimental and analytical investigation of meso-scale slug bubble dynamics in a square capillary channel, Physics of Fluids, 32(8) (2020) 083304.

[62] H. Wong, C. Radke, S. Morris, The motion of long bubbles in polygonal capillaries. Part 1. Thin films, Journal of Fluid Mechanics, 292 (1995) 71-94.

[63] R. Sander, Compilation of Henry's law constants (version 4.0) for water as solvent, Atmospheric Chemistry and Physics, 15(8) (2015) 4399-4981.

[64] J. Yue, L. Luo, Y. Gonthier, G. Chen, Q. Yuan, An experimental study of air–water Taylor flow and mass transfer inside square microchannels, Chemical Engineering Science, 64(16) (2009) 3697-3708.

[65] J. Yue, G. Chen, Q. Yuan, L.a. Luo, H. Le Gall, Mass transfer in gas-liquid flow in microchannels, Journal of Chemical Industry Engineering-China, 57(6) (2006) 1296.

[66] C. Li, C. Zhu, Y. Ma, D. Liu, X. Gao, Experimental study on volumetric mass transfer coefficient of CO2 absorption into MEA aqueous solution in a rectangular microchannel reactor, International Journal of Heat and Mass Transfer, 78 (2014) 1055-1059.

[67] H. Niu, L. Pan, H. Su, S. Wang, Effects of design and operating parameters on CO2 absorption in microchannel contactors, Industrial & Engineering Chemistry Research, 48(18) (2009) 8629-8634.

[68] G. Bercic, A. Pintar, The role of gas bubbles and liquid slug lengths on mass transport in the Taylor flow through capillaries, Chemical Engineering Science, 52(21-22) (1997) 3709-3719.

[69] C. Yao, Z. Dong, Y. Zhao, G. Chen, Gas-liquid flow and mass transfer in a microchannel under elevated pressures, Chemical Engineering Science, 123 (2015) 137-145.

[70] J. Van Baten, R. Krishna, CFD simulations of mass transfer from Taylor bubbles rising in circular capillaries, Chemical Engineering Science, 59(12) (2004) 2535-2545.

[71] T. Sherwood, R. Pigford, C. Wilke, Mass Transfer McGraw-Hill, New York, (1975).

[72] L.S. Liebovitch, T. Toth, A fast algorithm to determine fractal dimensions by box counting, physics Letters A, 141(8-9) (1989) 386-390.

[73] H. Li, T. Zhang, Imaging and characterizing fluid invasion in micro-3D printed porous devices with variable surface wettability, Soft Matter, 15(35) (2019) 6978-6987.

Printed by Media-Tryck, Lund 2022 NORDIC SWAN ECOLABEL 3041 0903

Department of Energy Sciences
Faculty of Engineering
Lund University

ISBN 978-91-8039-457-4
ISRN LUTMDN/TMHP-22/7108-SE
ISSN 0282-1990